

# Influence of geochemical features on the mechanical properties of organic matter in shale

Junliang Zhao<sup>1</sup>, Wei Zhang<sup>1</sup>, Dongxiao Zhang<sup>2</sup>, Ren Wei<sup>1</sup>, and Yuhan Wang<sup>1</sup>

<sup>1</sup>Peking University

<sup>2</sup>Southern University of Science and Technology

November 21, 2022

## Abstract

Organic matter is an important constituent in organic-rich shale, which influences the hydrocarbon generation, as well as the mechanical behavior, of shale reservoirs. The physical, chemical, and mechanical properties of organic matter depend on the source material and the thermal evolution process. Previous works attempted to investigate the impact of thermal maturation on the mechanical properties of organic matter. However, owing to the lack of maceral classification and the limitation of data volume during the mechanical measurement, no consistent trend has been identified. In this work, vitrinite reflectance test, scanning electron microscope observation, nanoindentation, and micro-Raman analysis were combined for geochemical and mechanical characterization. A total of 114 test areas were selected for testing, enhancing reliability of the test results. The Young's moduli of organic matter are from 3.57 GPa to 8.32 GPa. With the same thermal maturity, inertinite has the highest Young's modulus, while the modulus of bitumen is the lowest. The Young's moduli of different organic types all increase with vitrinite reflectance. When vitrinite reflectance increases from 0.62% to 1.13%, the modulus of inertinite and vitrinite is increased by 57% and 78%, respectively. In addition, with the increase of thermal maturity, the micro-Raman test results show a decrease of intensity ratio of D peak to G peak, indicating an increase of the ordered structure in organic matter. Organic type and thermal maturity reflect the diversity of the source material and chemical structure change during the thermal evolution process, and together they influence the mechanical properties of organic matter.

1  
2 **Influence of geochemical features on the mechanical properties of**  
3 **organic matter in shale**

4 **Junliang Zhao<sup>1</sup>, Wei Zhang<sup>1</sup>, Dongxiao Zhang<sup>2</sup>, Ren Wei<sup>3</sup>, and Yuhan Wang<sup>3</sup>**

5 <sup>1</sup>BIC-ESAT, ERE and SKLTCS, College of Engineering, Peking University, Beijing 100871, P.  
6 R. China.

7 <sup>2</sup>School of Environmental Science and Engineering, Southern University of Science and  
8 Technology, Shenzhen 518055, P. R. China.

9 <sup>3</sup>School of Earth and Space Sciences, Peking University, Beijing 100871, P. R. China.

10 Corresponding author: Dongxiao Zhang (zhangdx@sustech.edu.cn)

11 **Key Points:**

- 12 • Young's modulus of inertinite and vitrinite is much higher than that of bitumen
- 13 • Modulus of organic matter increases with thermal maturity
- 14 • Intensity ratio of D peak to G peak of inertinite's Raman spectrum exhibits a decreasing
- 15 trend with maturity

16  
17  
18

19 **Abstract**

20 Organic matter is an important constituent in organic-rich shale, which influences the  
21 hydrocarbon generation, as well as the mechanical behavior, of shale reservoirs. The physical,  
22 chemical, and mechanical properties of organic matter depend on the source material and the  
23 thermal evolution process. Previous works attempted to investigate the impact of thermal  
24 maturation on the mechanical properties of organic matter. However, owing to the lack of  
25 maceral classification and the limitation of data volume during the mechanical measurement, no  
26 consistent trend has been identified. In this work, vitrinite reflectance test, scanning electron  
27 microscope observation, nanoindentation, and micro-Raman analysis were combined for  
28 geochemical and mechanical characterization. A total of 114 test areas were selected for testing,  
29 enhancing reliability of the test results. The Young's moduli of organic matter are from 3.57 GPa  
30 to 8.32 GPa. With the same thermal maturity, inertinite has the highest Young's modulus, while  
31 the modulus of bitumen is the lowest. The Young's moduli of different organic types all increase  
32 with vitrinite reflectance. When vitrinite reflectance increases from 0.62% to 1.13%, the modulus  
33 of inertinite and vitrinite is increased by 57% and 78%, respectively. The indentation creep of  
34 different organic matter suggests that the stiffer organic type demonstrates less creep influence.  
35 In addition, with the increase of thermal maturity, the micro-Raman test results show a decrease  
36 of intensity ratio of D peak to G peak, indicating an increase of the ordered structure in organic  
37 matter. From the characterization results, it was found that organic type and thermal maturity  
38 reflect the diversity of the source material and the chemical structure change during the thermal  
39 evolution process, and together they influence the mechanical properties of organic matter.

40

41 **Keywords:** organic type; thermal maturity; organic matter; Young's modulus; shale.

## 42 **1. Introduction**

43 Organic-rich shale is not only the source rock of conventional reservoirs, but also the reservoir  
44 rock of shale oil/gas reservoirs. Organic matter is an important constituent in organic-rich shale,  
45 which distinguishes organic-rich shale from other mud rocks with low organic content, and  
46 significantly influences the exploration and development of shale oil/gas. On the one hand,  
47 kerogen is the source material of hydrocarbon, and total organic carbon (TOC) content is an  
48 essential index for the evaluation of geological sweet spots (Cudjoe et al., 2016; Naizhen and  
49 Guoyong, 2016). On the other hand, the mechanical properties that significantly affect the  
50 fracturing effect of shale are quite different for organic matter and inorganic minerals in shale.  
51 Consequently, many indices for the evaluation of engineering sweet spots, for example, the  
52 brittleness index (Rybacki et al., 2016; Wang and Carr, 2012; Zhao et al., 2018), are also related  
53 to organic matter.

54 Organic matter in shale comes from deposits of the dead bodies of ancient organisms, and it  
55 can be classified on the basis of the diversity of source organisms and sedimentary environments.  
56 According to solubility, organic matter can be divided into kerogen and bitumen (Hunt, 1979).  
57 Regarding kerogen, two classification schemes exist: optical classification and chemical  
58 classification. The optical classification scheme borrows methods and concepts from coal  
59 petrology (Hutton et al., 1994; Stach et al., 1982). Through reflected light analysis, kerogen can  
60 be classified into maceral groups, such as inertinite, vitrinite, and exinite. Chemical classification  
61 focuses on the content of C, H, and O elements in kerogen. By major chemical elements analysis,  
62 kerogen can be classified as type I, type II, and type III (Tissot and Welte, 2013). Optical  
63 classification and chemical classification schemes are related to each other (Hunt, 1979).  
64 However, optical classification usually measures organic matter in certain micro regions, while

65 chemical classification refers to characterization of the whole rock. In addition to organic type,  
66 thermal maturity constitutes another important geochemical property of organic matter. Thermal  
67 maturity indicates the thermal evolution and hydrocarbon generation stage of the source rock.  
68 Vitrinite reflectance is a key indicator of thermal maturity. Owing to the absence of higher  
69 plants, rocks prior to the Devonian period do not contain vitrinite. Consequently, researchers  
70 usually measure the reflectance of bitumen or graptolite as an alternative (Bertrand, 1990;  
71 Bertrand and Heroux, 1987; Jacob, 1989). Organic type and thermal maturity together influence  
72 the chemical structures of organic matter in shale.

73 Due to the lack of resolution, the elastic property of organic matter is difficult to characterize  
74 using conventional mechanical test methods. However, micromechanical test techniques, such as  
75 nanoindentation and modulus mapping based on nanoindenter and PeakForce quantitative  
76 nanomechanical mapping (QNM) by atomic force microscope (AFM), offer convenience of  
77 investigation at micro scale (Balooch et al., 2004; Dayal et al., 2009; Dokukin and Sokolov,  
78 2012). Mechanical characterization of organic matter in shale can be divided into two types. In  
79 the first type, organic matter was treated as a part of the main constituents in shale, and was  
80 directly characterized through the application of micromechanical test techniques (Alstadt et al.,  
81 2015; Bennett et al., 2015; Eliyahu et al., 2015; Kumar et al., 2012; Wilkinson et al., 2015;  
82 Zargari et al., 2013; Zeszotarski et al., 2004). The reported modulus of organic matter was  
83 generally between 0 GPa to 25 GPa, which was much lower than that of inorganic minerals.  
84 These researches revealed strong micromechanical heterogeneity within different constituents in  
85 organic-rich shales. In the second type, geochemical features of organic matter were taken into  
86 consideration (Emmanuel et al., 2016; Li et al., 2018; Zargari et al., 2016). Kerogen and bitumen  
87 with different thermal maturities were usually separated during the measurements. Previous

88 works in the second type suggested that the elastic modulus of organic matter is associated with  
89 organic type and thermal maturity. Owing to the lack of classification of kerogen and the  
90 limitation of data volume, however, no consistent trend has yet been discerned. Yang et al.  
91 (2017) measured the mechanical properties of different macerals in shale using AFM-based  
92 Nano IR. Inertinite, bitumen and tasmanite were separated in the work, but thermal maturity was  
93 not considered for mechanical characterization. Similar to characterization of organic matter in  
94 shale, the mechanical properties of macerals in coal and the influence of coal rank have also been  
95 studied (Borodich et al., 2015; Epshtein et al., 2015; Vranjes et al., 2018; Zhang et al., 2019).  
96 However, understanding of the exact influence requires further studies. In addition, molecular  
97 simulation has recently been utilized to investigate the structures and mechanical properties of  
98 organic matter (Bousige et al., 2016; Tong et al., 2016; Ungerer et al., 2014). The chemical  
99 structure of organic matter is very complex, and to precisely construct a molecular model, and  
100 predict the physical and mechanical properties, remain a challenge. Experimental works at micro  
101 and nano scales can provide a useful reference and validation for simulations.

102 In this study, four shale samples with different thermal maturities from the Bonan Sub-sag  
103 are prepared. A number of geochemical and micromechanical tests are combined to characterize  
104 the properties of organic matter in each sample. Vitrinite reflectance is measured using a  
105 photomicrometer. Inertinite, vitrinite, and bitumen are identified based on an optical  
106 classification scheme. Nanoindentation is performed to characterize the mechanical properties of  
107 organic matter in the selected test areas. Moreover, to elucidate the evolution of chemical  
108 structures of organic matter, micro-Raman test is carried out. Micromechanical test results are  
109 compared with the reported data. The influence of organic type and thermal maturity is discussed  
110 on the basis of the characterization results.

111

## 112 **2. Materials and methods**

### 113 2.1. Sample information and preparation

114 Samples used in this study are shale cores of the third member of the Shahejie Formation from  
115 the Bonan Sub-sag. The Bonan Sub-sag is a third-order tectonic unit in the central part of the  
116 Zhanhua Depression in the Bohai Bay Basin with an area of 600 km<sup>2</sup>. During the Paleogene  
117 period, the Bohai Bay Basin experienced initial, developmental, prosperous and atrophic periods  
118 of the fault depression, and successively developed the Kongdian Formation, the Shahejie  
119 Formation, and the Dongying Formation (Jiu et al., 2013; Wang et al., 2015). The Shahejie  
120 Formation can be divided into four sub-sections, and the third member of the Shahejie Formation  
121 from the Bonan Sub-sag contains a large number of shale oil formations.

122 Shale pieces with thicknesses from 2 mm to 5mm were cut from the shale cores. Then,  
123 mechanical polishing was performed to keep the upper and lower surface of the shale pieces  
124 parallel to each other, and to primarily decrease surface roughness. Finally, the upper surface  
125 was subjected to ion polishing to further decrease roughness. The roughness of a 20 μm × 20 μm  
126 area in the sample surface is below 100 nm.

### 127 2.2. Characterization methods

#### 128 2.2.1. Vitrinite reflectance test

129 The vitrinite reflectance test is an effective method to characterize the thermal maturity of  
130 organic matter. The device for the vitrinite reflectance test, the photomicrometer, is a  
131 combination of an optical microscope and a spectrophotometer. The optical microscope with an  
132 oil immersion objective is utilized for observation and test area selection. The spectrophotometer  
133 is used to measure reflectance in a certain area. In addition to the vitrinite reflectance test, a

134 photomicrometer can also assist with optical classification of organic types according to image  
135 contrast and reflectance data. The reflectance test and optical microscope observation, which  
136 determine thermal maturity and organic type, constitute the foundation of the following tests.

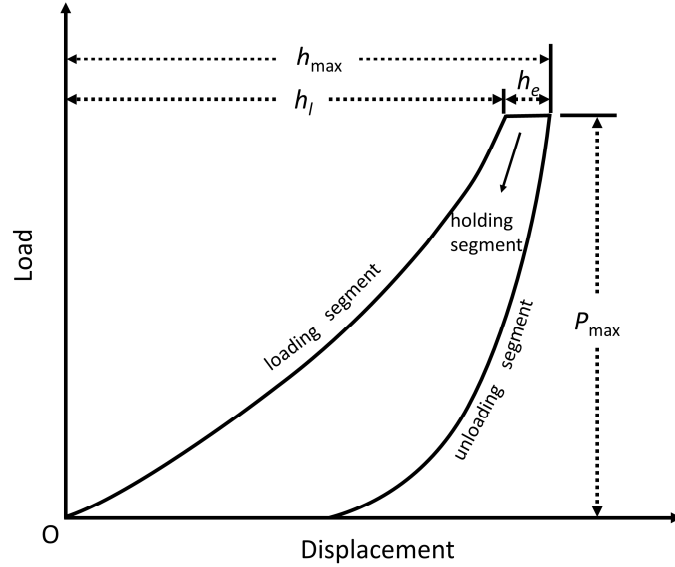
#### 137 2.2.2. Micro-Raman test

138 Raman spectrum is very sensitive to the structure and molecular arrangement of carbon  
139 materials. Raman spectrum analysis is widely employed for characterization of carbon materials,  
140 such as carbon nanotube and graphene (Dresselhaus et al., 2005; Ferrari et al., 2006; Pimenta et  
141 al., 2007). Numerous researchers have also performed Raman spectrum tests on organic matter in  
142 source rocks, and attempted to correlate the spectrum features with the results from conventional  
143 vitrinite reflectance tests, to develop novel methods for the determination of thermal maturity  
144 (Kelemen and Fang, 2001; Wilkins et al., 2014). Two ways of Raman spectrum analysis exist for  
145 organic matter in shale. The first one needs to extract organic matter from shale rocks by  
146 mechanical and chemical purification methods. However, this way necessitates destruction of the  
147 shale rock during purification, which makes it unusable for mechanical tests. The second way is  
148 via a micro-Raman test. Similar to the photometric test, micro-Raman combines optical  
149 observation and Raman spectrum analysis (Lünsdorf, 2016; Tselev et al., 2014), which can  
150 locate the micro areas and perform the measurements. Due to its advantages, the second way is  
151 chosen for this study.

#### 152 2.2.3. Nanoindentation

153 Mainstream commercial nanoindenters are developed on the basis of the method proposed by  
154 Oliver and Pharr (Oliver and Pharr, 1992; Oliver and Pharr, 2004). During the nanoindentation  
155 measurement, an indenter with a certain geometry is penetrated into the sample surface until the

156 targeted force or depth, and then it is pulled out. The load  $P$  on the sample and the displacement  
 157  $h$  of the indenter tip are recorded in the loading, holding, and unloading process (Figure 1).



158  
 159 **Figure 1.** A schematic representation of load-displacement curve from nanoindentation.  $P_{\max}$  is  
 160 the peak load;  $h_{\max}$  is the maximum indenter displacement;  $h_l$  is the displacement at the end of  
 161 the loading segment; and  $h_e$  is the displacement increase during the holding process.

162 The unloading segment of the  $P$ - $h$  curve reflects the elastic properties of the sample material.  
 163 According to the contact mechanics (Pharr et al., 1992), the basic model for nanoindentation is as  
 164 follows:

$$165 \quad E_r = \frac{\sqrt{\pi}}{2} \frac{S}{\sqrt{A}} \quad (1)$$

166 where  $E_r$  is the reduced modulus;  $S$  is the slope of the initial unloading segment; and  $A$  is the  
 167 contact area of the indenter tip on the sample surface, which can be determined by the corrected  
 168 area function (Oliver and Pharr, 1992):

$$169 \quad A = 24.5h_c^2 + \sum_{i=0}^7 C_i h_c^{1/2^i} \quad (2)$$

170 where  $C_i$  are fitting parameters; and  $h_c$  is the contact depth of the indenter, which is related to the  
 171 maximum displacement  $h_{\max}$  (Oliver and Pharr, 1992):

$$172 \quad h_c = h_{\max} - \beta \frac{P_{\max}}{S} \quad (3)$$

173 where  $\beta$  is the parameter corresponding to the geometry of the indenter; and  $P_{\max}$  is the peak  
 174 load. The reduced modulus is determined by both the sample and the indenter material. The  
 175 following equation can be used to eliminate the influence from the indenter and calculate the  
 176 Young's modulus  $E$  of the sample (Johnson, 1987):

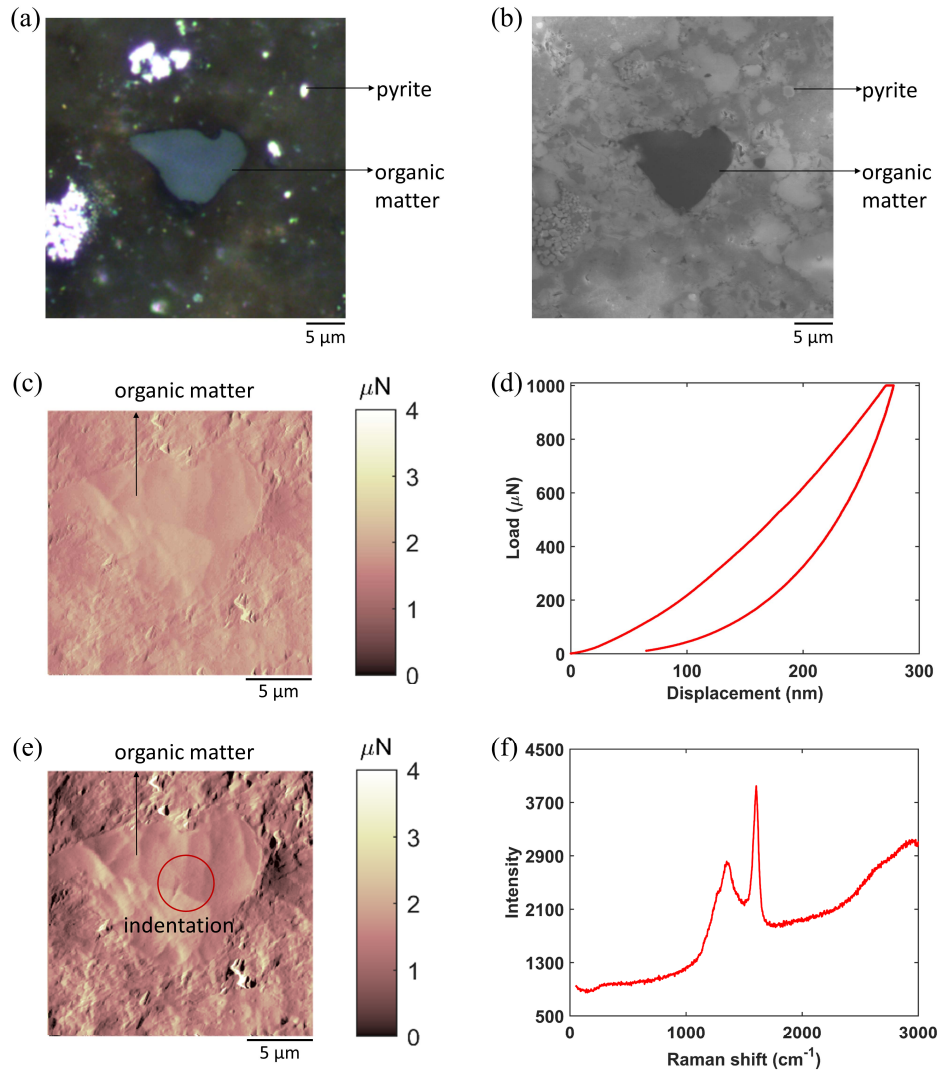
$$177 \quad \frac{1 - \gamma^2}{E} = \frac{1}{E_r} - \frac{1 - \gamma_{tip}^2}{E_{tip}} \quad (4)$$

178 where  $\gamma$  is the Poisson's ratio of the sample; and  $E_{tip}$  and  $\gamma_{tip}$  are the Young's modulus and  
 179 Poisson's ratio of the indenter tip, respectively.

#### 180 2.2.4. Experimental procedures

181 Geochemical test and mechanical characterization are combined in this study (Figure 2). Ion-  
 182 polished samples were placed into a photomicrometer (QDI 302, CRAIC; DM4500P, Leica).  
 183 Test areas containing organic matters were observed and selected under an oil immersion  
 184 objective (Figure 2a). The spectrophotometer was used to measure the reflectance of organic  
 185 matter. The illumination spot size for reflectance measurement was approximately 3  $\mu\text{m}$ . Organic  
 186 type was identified through optical image and reflectance data. Vitrinite reflectance constitutes  
 187 the measurement of the thermal maturity of each sample. SEM observation (Figure 2b) was then  
 188 carried out to observe the selected test areas at a low vacuum condition with an accelerate  
 189 voltage of 15 kV (Quanta 200F, FEI). For convenience of positioning in the following  
 190 procedures, the precise coordinate of each test area was recorded, and SEM images of organic  
 191 matters were captured at various magnifications. Subsequently, the elastic properties of organic

192 matter in each sample were measured using nanoindentation (Tribo Indenter 950, Hysitron).  
193 Scanning probe microscopy (SPM) was performed prior to (Figure 2c) and after (Figure 2e)  
194 nanoindentation, to determine the indentation position and to observe the residual indentation,  
195 respectively. The indentation was usually placed at the center position of organic matter to avoid  
196 the interference from surrounding minerals. A Berkovich diamond indenter with a nominal tip  
197 radius of 100 nm was chosen for the test. Under load controlling mode, the maximum load was  
198 set to be 1000  $\mu\text{N}$  (Figure 2d), which was uniform for each indentation. The loading, holding,  
199 and unloading time were set to be 10 s, 2 s and 10 s, respectively. The contact area of the  
200 indentation was on the order of  $10^6 \text{ nm}^2$ . Finally, the micro-Raman test (Figure 2f) was  
201 performed to elucidate the structural variation within the organic matter with different thermal  
202 maturities (DXRxi, ThermoFisher). The immersion source was a 532 nm laser, and the exposure  
203 time was 0.05 s. The spot size of the laser beam was about 1  $\mu\text{m}$ . To decrease damage on the  
204 sample surface, the laser power was set to be 0.5 mW.



205

206 **Figure 2.** Experimental procedures: (a) Vitrinite reflectance test, macerals classification, and test  
 207 area selection; (b) SEM observation and test area location; (c) SPM (scanning frequency = 0.2  
 208 Hz) observation prior to nanoindentation; (d) nanoindentation; (e) SPM (scanning frequency =  
 209 0.5 Hz) observation after nanoindentation; and (f) micro-Raman analysis.

### 210 3. Results and discussion

#### 211 3.1. Organic type and thermal maturity

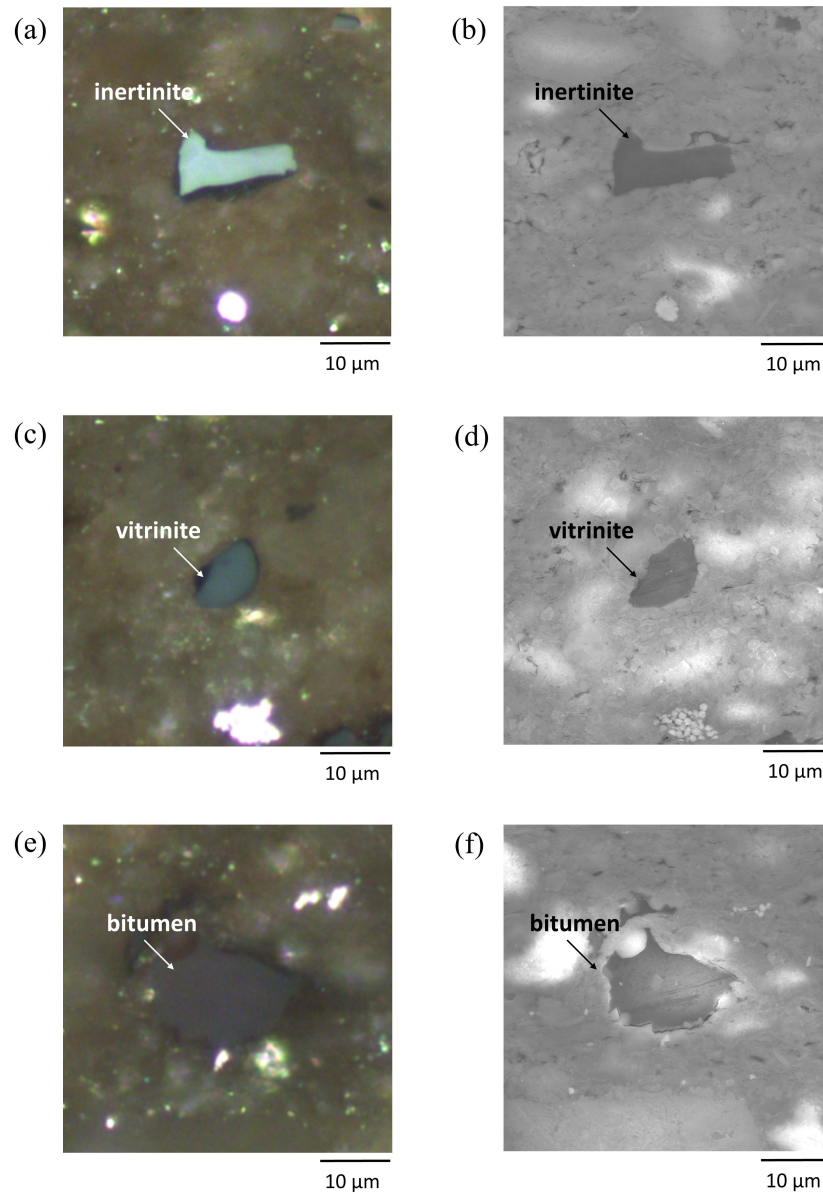
212 Table 1 shows the organic type classification and thermal maturity test results. The vitrinite  
 213 reflectance of shale samples is from 0.62% to 1.13%, which means that all of the samples are in

214 the mature stage. According to the image features under the oil immersion objective, three  
 215 organic types, including vitrinite, inertinite and bitumen, are identified in the shale samples.

216 **Table 1.** Vitrinite reflectance and number of areas tested in each sample.

Sample	R <sub>o</sub> (%)	Number of areas tested		
		Vitrinite	Inertinite	Bitumen
J1	0.62	16	11	—
J2	0.69	12	9	15
J3	0.94	10	11	6
J4	1.13	9	12	3

217  
 218 Figure 3 compares the optical images and SEM images of different organic types. Compared  
 219 with the dry objective, the oil immersion objective can greatly increase the image contrast and  
 220 the clarity of organic matter. Through the first column of Figure 3, one can see that the image  
 221 features of the typical test areas are markedly different. Specifically, the organic type in the first  
 222 test area is inertinite, which is cinerous and seems to protrude from the sample surface (Figure  
 223 3a). In contrast, vitrinite in the second test area (Figure 3c) and bitumen in the last test area  
 224 (Figure 3e) are dark gray and brown, respectively. However, it is challenging to differentiate the  
 225 organic types based only on the image contrast of SEM images (Figure 3b, d, f). In addition to  
 226 optical images, the reflectance test results can also assist with the classification of organic type.  
 227 The reflectance of vitrinite is usually higher than the reflectance of bitumen, while lower than  
 228 that of inertinite. In sample J2, for example, bitumen reflectance is from 0.39% to 0.52%,  
 229 vitrinite reflectance is from 0.46% to 1.1%, and inertinite reflectance is from 1.1% to 2.2%. A  
 230 total of 114 test areas that contain different types of organic matter are selected for  
 231 nanoindentation test (Table 1).



232

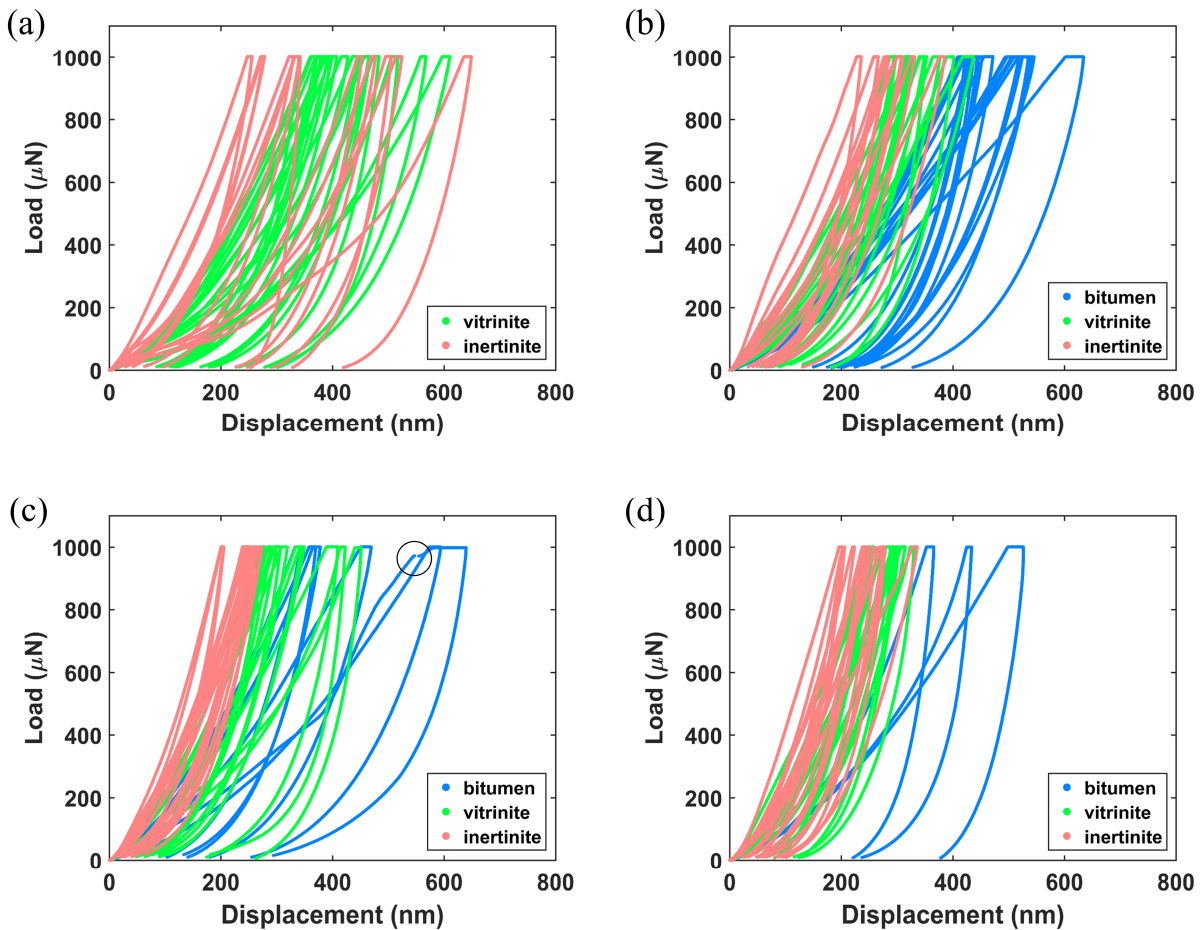
233 **Figure 3.** Different types of organic matter in sample J3: (a) Optical image and (b) SEM image  
234 of inertinite; (c) optical image and (d) SEM image of vitrinite; and (e) optical image and (f) SEM  
235 image of bitumen.

### 236 3.2. Nanoindentation results

237 The number of areas tested of each kind of organic matter in each sample is listed in Table 1.

238 Figure 4 assembles the  $P$ - $h$  curves for different kinds of organic matter in each sample. With the

239 same maximum load setting, the maximum displacement of vitrinite is generally lower than that  
 240 of inertinite, while higher than that of bitumen. The sudden increase of displacement during the  
 241 loading process in Figure 4c, which is marked with a black circle, is termed *pop-in*. It suggests  
 242 the rapture of organic matter. The comparison of the *P-h* curves indicates that bitumen is much  
 243 softer than vitrinite and inertinite with the same thermal maturity.

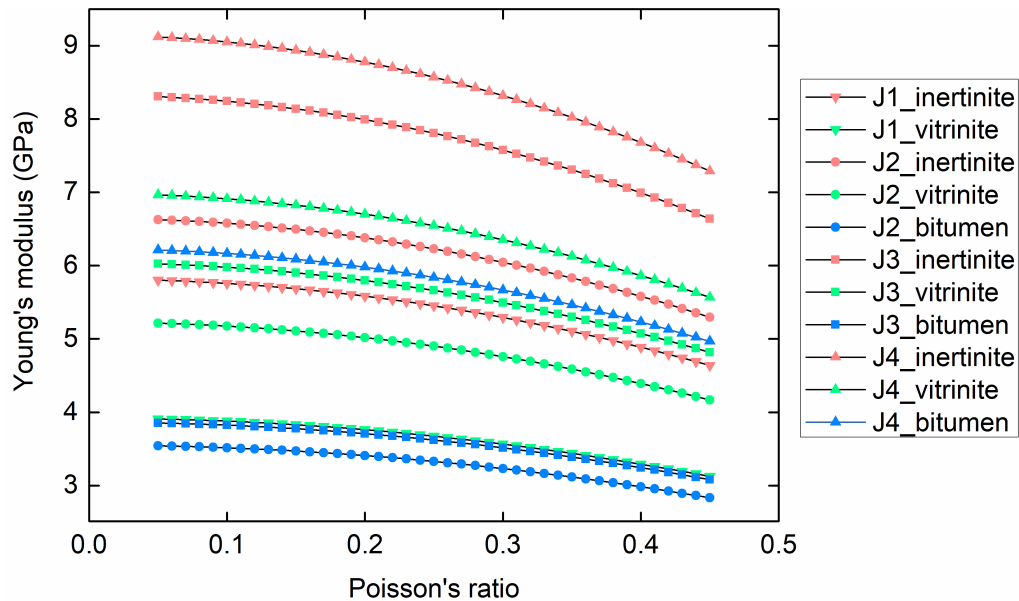


244

245 **Figure 4.** Assembly of representative *P-h* curves from sample J1 (a), J2 (b), J3 (c), and J4 (d).

246 The Young's modulus can be calculated using equation (1) to equation (4). The Young's  
 247 modulus and Poisson's ratio of the diamond indenter tip are 1141 GPa and 0.07, respectively.  
 248 However, the Poisson's ratio of organic matter remains unknown, and the estimation of  
 249 Poisson's ratio influences the calculation results. A wide range of Poisson's ratio of organic

250 matter, from 0.05 to 0.45, was used in previous literature (Ahmadov et al., 2009; Eliyahu et al.,  
 251 2015; Emmanuel et al., 2016; Li et al., 2018). Figure 5 illustrates the sensitivity to Poisson's  
 252 ratio based on the load-displacement data in this work. The calculated Young's modulus of  
 253 organic matter gradually increases with the selected Poisson's ratio value. In the following  
 254 discussions, the Poisson's ratio of organic matter is assumed to be 0.3. The maximum  
 255 uncertainty introduced by the assumption is approximately 12.4%.



256

257 **Figure 5.** The sensitivity of calculated Young's modulus to Poisson's ratio of organic matter.

258 Table 2 summarizes Young's modulus calculation results. It is obvious that inertinite has  
 259 the highest Young's modulus, while the modulus of bitumen is the lowest. Moreover, the  
 260 Young's moduli of different organic types all increase with vitrinite reflectance. When vitrinite  
 261 reflectance increases from 0.62% to 1.13%, the Young's modulus of inertinite increases from  
 262 5.29 GPa to 8.32 GPa, by 57%, and the Young's modulus of vitrinite increases from 3.57 GPa to  
 263 6.35 GPa, by 78%. From Table 2, it can be concluded that both organic type and thermal  
 264 maturity affect the mechanical properties of organic matter. Repeated testing on a number of test  
 265 areas (Table 1) for different organic types in each sample provides a valuable dataset to examine

266 the variability of the mechanical properties and the reliability of the test results. Except for a  
 267 couple of test results (i.e., inertinite for sample J1 and bitumen for J3), the standard deviation for  
 268 each type of testing is moderate (Table 2), indicating either a reliable testing result or moderate  
 269 variability, or both.

270 **Table 2.** Young's modulus of different types of organic matter.

Sample	R <sub>o</sub> (%)	Young's modulus (GPa) <sup>a</sup>		
		Vitrinite	Inertinite	Bitumen
J1	0.62	3.57±0.83	5.29±2.85	—
J2	0.69	4.76±0.85	6.05±1.63	3.23±0.80
J3	0.94	5.50±0.80	7.58±1.38	3.52±1.25
J4	1.13	6.35±0.97	8.32±1.53	5.67±0.84

271 <sup>a</sup>± indicates the standard deviation.

272 An increase in displacement in the holding segment (Figure 4) indicates the viscoelasticity  
 273 of organic matter, which was also investigated in previous works (Epshtein et al., 2015; Liu et al.,  
 274 2019; Zeszotarski et al., 2004). To discuss the problem, indentation creep  $C_{IT}$  is calculated by  
 275 using the following equation (ISO14577-1, 2002):

$$276 \quad C_{IT} = \frac{h_e}{h_l} \times 100 \quad (5)$$

277 where  $h_e$  and  $h_l$  are the displacement increase during the holding and loading process,  
 278 respectively. The  $C_{IT}$  values of different types are summarized in Table 3. With the same  
 279 maximum load and holding time setting, the indentation creep of bitumen is much higher than  
 280 that of vitrinite and inertinite. The calculation results suggest that the stiffer organic type  
 281 demonstrates less creep influence. However, no clear relation is identified between indentation  
 282 creep and thermal maturity. While this work focuses on the elastic properties of organic matter, a  
 283 longer holding time and more suitable test method, for example, dynamic mechanical analysis,

284 would be required for rigorous study of the creep behavior (Chagnon et al., 2013; Koch et al.,  
285 2007).

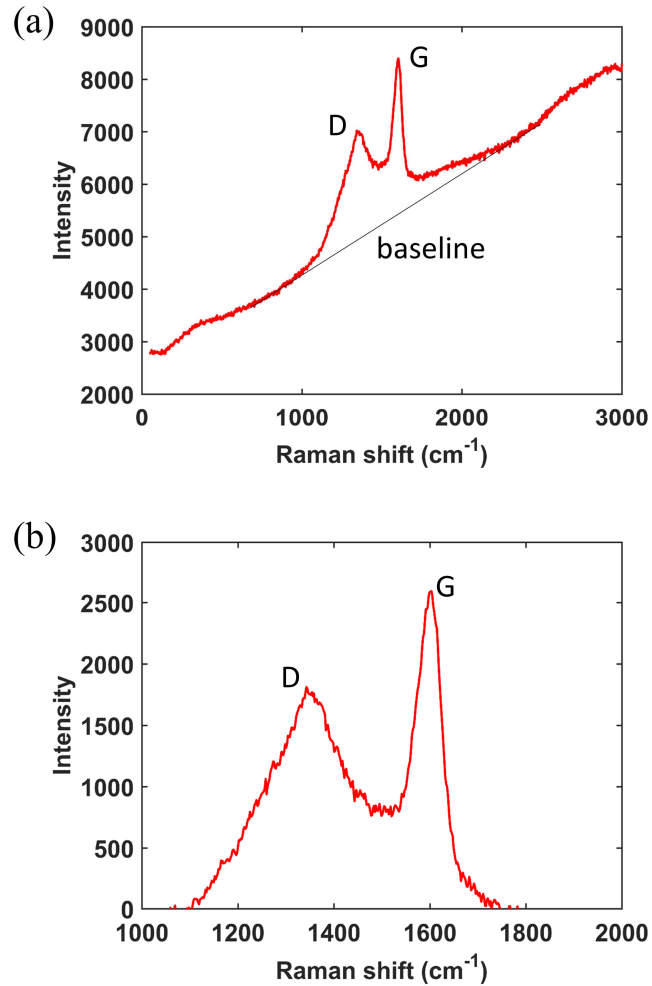
286 Table 3. Indentation creep calculation results.

Sample	R <sub>o</sub> (%)	Indentation creep (%) <sup>a</sup>		
		Vitrinite	Inertinite	Bitumen
J1	0.62	2.40±0.31	2.21±0.62	—
J2	0.69	3.09±0.73	2.65±0.81	4.61±1.11
J3	0.94	2.97±1.00	2.18±0.51	4.66±2.87
J4	1.13	2.38±0.75	2.18±0.59	3.77±1.76

287 <sup>a</sup>± indicates the standard deviation.

### 288 3.3. Micro-Raman analysis

289 Because of the influence from fluorescence, the Raman spectrum of bitumen and vitrinite has a  
290 poor signal-to-noise ratio, and we can only obtain reliable data about inertinite. Through  
291 processing of the original spectrum, the micro-Raman test results are analyzed. Figure 6  
292 illustrates a typical Raman spectrum of inertinite. There is a strong fluorescence background in  
293 the original Raman data (Figure 6a). Similar to the carbon materials, two characteristic peaks in  
294 the spectrum are observed. To remove the background, the baseline is calculated by using the  
295 data points around the characteristic peaks. In Figure 6b, the peak around 1350 cm<sup>-1</sup> is the defect  
296 peak (D peak), which indicates the defects and the disordered structure in the material. The peak  
297 around 1600 cm<sup>-1</sup> is the graphene peak (G peak), which originates from the plane structure of  
298 carbon materials. The intensity ratio of D peak to G peak (IR (D/G)) can be the indicator of the  
299 degree of graphitization. A higher IR (D/G) indicates fewer defects, a smaller disordered  
300 structure, and a higher degree of graphitization.



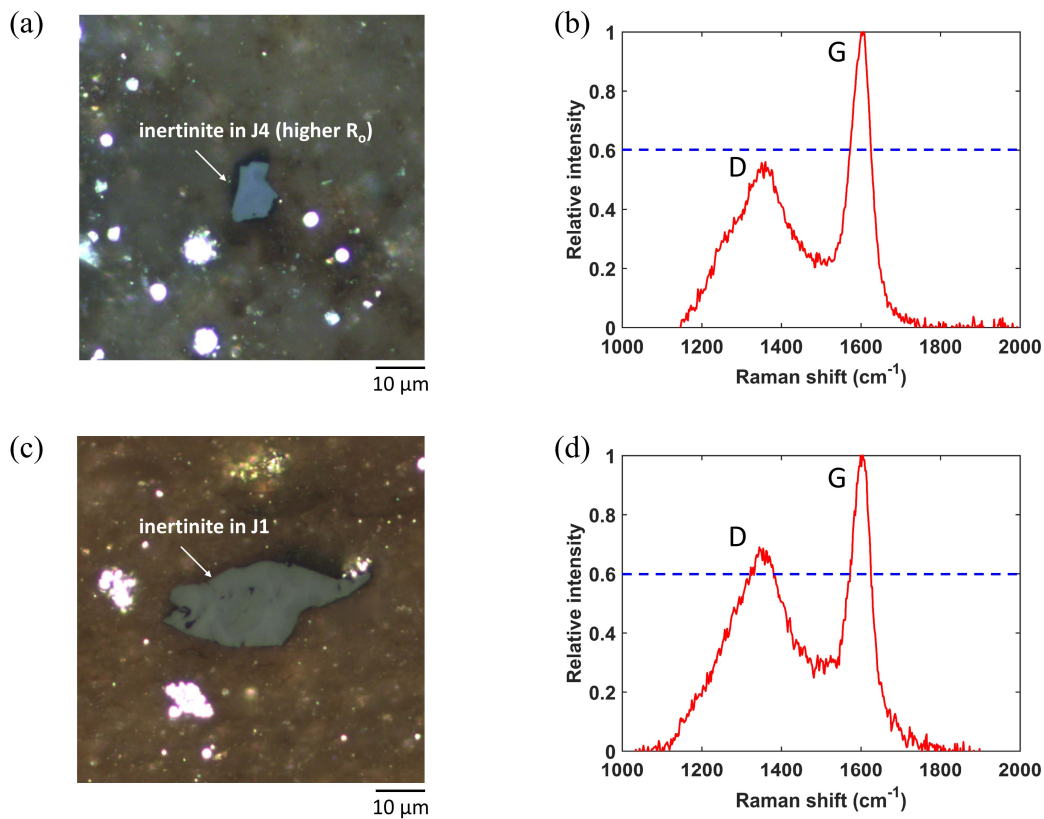
301

302 **Figure 6.** Data processing of Raman spectrum: (a) Original Raman spectrum of inertinite with  
 303 strong fluorescence background; and (b) processed spectrum in the region of interest. D and G  
 304 indicate characteristic peaks in the Raman spectrum of carbon material. The baseline is  
 305 calculated by using the data points around the characteristic peaks. The intensity ratio of D peak  
 306 to G peak is calculated through the division of maximum intensity value of the D band to that of  
 307 the G band.

308

309 Figure 7 compares two representative Raman spectrums from sample J1 and J4,  
 310 respectively. The IR (D/G) of the inertinite in sample J1 is higher than that of the inertinite in

311 sample J4, which suggests that the organic matter in sample J4 has a higher degree of  
312 graphitization. The IR (D/G) of each sample is averaged (Table 4) in consideration of the  
313 heterogeneity within different inertinites in a certain shale sample. When vitrinite reflectance  
314 increases, the IR (D/G) exhibits a general decreasing trend. The chemical structure change  
315 results from thermal evolution. With the increase of thermal maturity, the aliphatic structure is  
316 gradually decomposed, and the aromaticity of kerogen increases (Craddock et al., 2018; Duan et  
317 al., 2018; Tissot and Welte, 2013). Therefore, the calculation results reveal that the organic  
318 matter with a higher thermal maturity may contain fewer defects and a more ordered structure.



319

320 **Figure 7.** Representative inertinite area and corresponding Raman spectrum from sample J4 (a,

321 b) and J1 (c, d).

322

323

324

**Table 4.** Intensity ratio of D peak to G peak of different samples.

Sample	R <sub>o</sub> (%)	IR (D/G) <sup>a</sup>	Number of areas tested
J1	0.62	0.648±0.024	11
J2	0.69	0.667±0.022	9
J3	0.94	0.620±0.038	11
J4	1.13	0.600±0.034	12

325 <sup>a</sup>± indicates the standard deviation.

## 326 3.4. Comparison with extant literature

327 Table 5 presents a comparison of the test results in this study and the reported data. In previous  
328 works, utilization of dynamic test techniques is preferred for mechanical characterization,  
329 including modulus mapping by nanoindentation system and QNM by AFM. Kerogen and  
330 bitumen are distinguished in previous research, but the macerals are not classified. Although  
331 Zargari et al. (2016) and Li et al. (2018) both investigate organic matter in Bakken shale, the test  
332 results show different trends. Zargari et al. (2016) find the modulus reduction of kerogen from  
333 immature to mature stage, while Li et al. (2018) observe that organic matter becomes stiffer as  
334 thermal maturity increases. The different findings may be owing to the lack of classification of  
335 organic type and the limited data volume. The test results provided by Zargari et al. (2016) are  
336 storage moduli, which are measured by using modulus mapping with a diamond indenter.  
337 Storage modulus is comparable to reduced modulus, and is also influenced by both the sample  
338 and the indenter tip (Zhao et al., 2018). The relation between storage modulus and Young's  
339 modulus is in the same form as equation (4) (Syed Asif et al., 2001), and the Young's modulus  
340 of diamond is much higher than that of organic matter. Thus, storage modulus and converted  
341 Young's modulus should have the same trend from immature to mature stage. The conclusion by  
342 Emmanuel et al. (2016) is that the modulus of kerogen significantly increases when vitrinite

343 reflectance increases from 0.40% to 0.82%, while the modulus hardly changes when vitrinite  
344 reflectance increases from 0.82% to 1.25%. However, in this paper, we find that the elastic  
345 modulus of vitrinite, inertinite, and bitumen all increase with thermal maturity.

346 Different from the previous investigations listed in Table 5, this study considers the  
347 influence of not only thermal maturity, but also organic type. Vitrinite and inertinite are  
348 identified based on optical microscope images and reflectance data. The difference of elastic  
349 properties between vitrinite and inertinite are found by nanoindentation measurements.  
350 Consequently, without consideration of maceral classification, conclusions about the influence  
351 from thermal maturity may be unreliable, especially when the data volume is limited. In addition,  
352 most of the previous investigations divide the shale samples into two parts. One is for  
353 geochemical characterization, while the other one is for the mechanical test. Sample-to-sample  
354 variation is also not adequately considered. In this work, a set of geochemical-mechanical  
355 experiments is performed on the same selected test areas in a certain sample. Sample-to-sample  
356 variation no longer presents a problem, and the experimental data of repeated tests on the same  
357 type of test areas provide meaningful statistics. Finally, micromechanical tests on shale are very  
358 time consuming, due to the complexity of sample preparation and locating the test area. The  
359 number of areas tested in previous works is also relatively small. Here, the data volume is  
360 significantly increased, which makes the test results in this work more reliable.

361

362

363

364

365

366

367

**Table 5.** Comparison with the test results in previous works.

Reference	R <sub>o</sub> (%)	Modulus (GPa)			Test technique	Number of areas tested
		Kerogen		Bitumen		
		Vitrinite	Inertinite			
Zargari et al. (2016) <sup>a</sup>	Immature	15~20	—	Modulus mapping	12	
	Mature	7~10	—			
	Mature	7~10	—			
	Overmature	7~12	—			
Emmanuel et al. (2016) <sup>b</sup>	0.40	6.10	—	AFM	26	
	0.82	16.0	7.50			
	1.25	15.80	8.50			
Li et al. (2018) <sup>c</sup>	0.35	2.91	—	AFM	3	
	0.64	—	3.33			
	1.04	—	11.77			
This work <sup>d</sup>	0.62	3.57	5.29	Nano-indentation	114	
	0.69	4.76	6.05			
	0.94	5.50	7.58			
	1.13	6.35	8.32			

368 <sup>a</sup>Modulus in this literature is storage modulus;369 <sup>b</sup>Modulus in this literature is Young's modulus;370 <sup>c</sup>Modulus in this literature is Young's modulus;371 <sup>d</sup>Modulus in this work is Young's modulus.

372

373 **4. Conclusions**

374 In the present paper, the influence of geochemical features on the mechanical properties of  
375 organic matter is investigated by combining various geochemical and micromechanical  
376 characterization methods. The relations between the mechanical properties of different organic  
377 types and thermal maturities are summarized in Figure 8. The main findings are as follows:

378 (1) Inertinite, vitrinite, and bitumen show different image features under the oil immersion  
379 objective and have a different reflectance range. It is difficult to distinguish organic type only  
380 according to the image contrast of SEM images.

381 (2) The vitrinite reflectance of the four shale samples is from 0.62% to 1.13%. With the same  
382 thermal maturity, mechanical heterogeneity exists within different types of organic matter.  
383 Inertinite has the highest Young's modulus, while the modulus of bitumen is the lowest. Taking  
384 sample J3 as an example, the Young's modulus of inertinite is more than two times that of the  
385 modulus of bitumen.

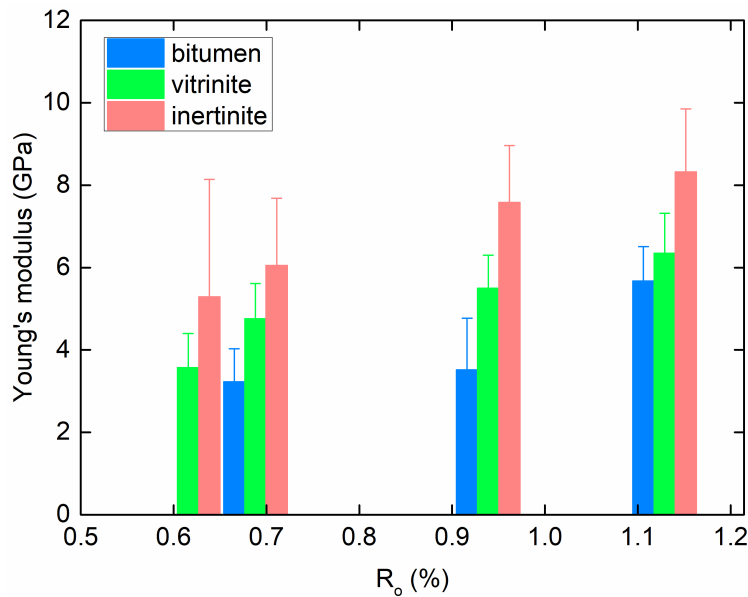
386 (3) The Young's moduli of all types of organic matter increase with thermal maturity. When  
387 vitrinite reflectance increases from 0.62% to 1.13%, the Young's modulus of inertinite increases  
388 from 5.29 GPa to 8.32 GPa, by 57%, and the Young's modulus of vitrinite increases from 3.57  
389 GPa to 6.35 GPa, by 78%. The indentation creep calculation results suggest that the stiffer  
390 organic type indicates less creep influence.

391 (4) Characteristic peaks of carbon material can be found in the Raman spectrum of inertinite. The  
392 intensity ratio of D peak to G peak exhibits a decreasing trend with thermal maturity, indicating  
393 the increase of graphitization degree of organic matter.

394 (5) The geochemical and micromechanical characterization results reveal that the mechanical  
395 properties of organic matter are influenced by both organic type and thermal maturity. Compared  
396 with bitumen, vitrinite and inertinite have more polycyclic aromatic hydrocarbons, fewer  
397 saturated aliphatic hydrocarbons, and higher carbon content. Therefore, with the same thermal  
398 maturity, the Young's modulus of vitrinite and inertinite is higher than that of bitumen. With the  
399 increase of thermal maturity, the aliphatic structure is gradually decomposed and consumed, and

400 the aromaticity of kerogen increases. Consequently, IR (D/G) decreases, and the Young's  
 401 modulus increases.

402 (6) The mechanical behavior of organic matter plays an important role in the predictions of  
 403 macroscopic mechanical properties at the core scale and even the well scale, especially for  
 404 organic-rich shales. This can be done based on upscaling methods, such as the Mori-Tanaka  
 405 model and the self-consistence method, with the mechanical characterization results of the main  
 406 constituents in shale (Abedi et al., 2016; Goodarzi et al., 2017; Zhao et al., 2018). The  
 407 characterization in this work can serve as a supplement to micro constituent input databases for  
 408 more reliable overall calculation results. At micro scale, the experimental research can also  
 409 provide validation for related molecular simulations (Bousige et al., 2016; Wu and Firoozabadi,  
 410 2020). In addition, mechanical variation within organic matters has the potential to inversely  
 411 assist with the identification of organic type and the determination of thermal maturity.



412

413 **Figure 8.** Young's modulus of organic matter with different vitrinite reflectance.

414 Considering sample-to-sample variation, this work proposes a workflow focusing on fixed  
 415 micro areas for different characterization. The data volume is also significantly increased

416 compared with that in the extant literature. However, the range of vitrinite reflectance in this  
417 study is limited, and all of the four samples are in the mature stage. In the future, shale samples  
418 in other thermal maturation stages need to be investigated.

419

## 420 **Acknowledgements**

421 This work is partially funded by the National Natural Science Foundation of China (Grant No.  
422 51520105005 and U1663208) and the National Science and Technology Major Project of China  
423 (Grant No. 2016ZX05034001-007, 2017ZX05009-005, and 2017ZX05049-003). The data used  
424 in this paper are available through the following link: <http://dx.doi.org/10.17632/hh22sgnnv4.1>.

425

## 426 **References**

- 427 Abedi, S., Slim, M., & Ulm, F.-J. (2016). Nanomechanics of organic-rich shales: the role of thermal maturity and  
428 organic matter content on texture. *Acta Geotechnica*, *11*(4), 775-787. <https://doi.org/10.1007/s11440-016-0476-2>
- 429 Ahmadov, R., Vanorio, T., & Mavko, G. (2009). Confocal laser scanning and atomic-force microscopy in estimation  
430 of elastic properties of the organic-rich Bazhenov Formation. *The Leading Edge*, *28*(1), 18-23.  
431 <https://doi.org/10.1190/1.3064141>
- 432 Alstadt, K. N., Katti, K. S., & Katti, D. R. (2015). Nanoscale morphology of kerogen and in situ nanomechanical  
433 properties of green river oil shale. *Journal of Nanomechanics and Micromechanics*, *6*(1), 04015003.  
434 [https://doi.org/10.1061/\(ASCE\)NM.2153-5477.0000103](https://doi.org/10.1061/(ASCE)NM.2153-5477.0000103)
- 435 Balooch, G., Marshall, G., Marshall, S., Warren, O., Asif, S. S., & Balooch, M. (2004). Evaluation of a new modulus  
436 mapping technique to investigate microstructural features of human teeth. *Journal of Biomechanics*, *37*(8), 1223-  
437 1232. <https://doi.org/10.1016/j.jbiomech.2003.12.012>
- 438 Bennett, K. C., Berla, L. A., Nix, W. D., & Borja, R. I. (2015). Instrumented nanoindentation and 3D mechanistic  
439 modeling of a shale at multiple scales. *Acta Geotechnica*, *10*(1), 1-14. <https://doi.org/10.1007/s11440-014-0363-7>
- 440 Bertrand, R. (1990). Correlations among the reflectances of vitrinite, chitinozoans, graptolites and scolecodonts.  
441 *Organic Geochemistry*, *15*(6), 565-574. [https://doi.org/10.1016/0146-6380\(90\)90102-6](https://doi.org/10.1016/0146-6380(90)90102-6)

- 442 Bertrand, R., & Heroux, Y. (1987). Chitinozoan, graptolite, and scolecodont reflectance as an alternative to vitrinite  
443 and pyrobitumen reflectance in Ordovician and Silurian strata, Anticosti Island, Quebec, Canada. *AAPG Bulletin*,  
444 *71*(8), 951-957. <https://doi.org/10.1306/948878f7-1704-11d7-8645000102c1865d>
- 445 Borodich, F. M., Bull, S., & Epshtein, S. (2015). Nanoindentation in studying mechanical properties of  
446 heterogeneous materials. *Journal of Mining Science*, *51*(3), 470-476. <https://doi.org/10.1134/s1062739115030072>
- 447 Bousige, C., Ghimbeu, C. M., Vix-Guterl, C., Pomerantz, A. E., Suleimenova, A., Vaughan, G., Garbarino, G.,  
448 Feygenson, M., Wildgruber, C., & Ulm, F.-J. (2016). Realistic molecular model of kerogen's nanostructure. *Nature*  
449 *Materials*, *15*(5), 576-582. <https://doi.org/10.1038/nmat4541>
- 450 Chagnon, L., Arnold, G., Giljean, S., & Brogly, M. (2013). Elastic recovery and creep properties of waterborne two-  
451 component polyurethanes investigated by micro-indentation. *Progress in Organic Coatings*, *76*(10), 1337-1345.  
452 <https://doi.org/10.1016/j.porgcoat.2013.04.003>
- 453 Craddock, P. R., Bake, K. D., & Pomerantz, A. E. (2018). Chemical, molecular, and microstructural evolution of  
454 kerogen during thermal maturation: case study from the Woodford Shale of Oklahoma. *Energy & Fuels*, *32*(4),  
455 4859-4872. <https://doi.org/10.1021/acs.energyfuels.8b00189>
- 456 Cudjoe, S., Vinassa, M., Gomes, J. H. B., & Barati, R. G. (2016). A comprehensive approach to sweet-spot mapping  
457 for hydraulic fracturing and CO<sub>2</sub> huff-n-puff injection in Chattanooga shale formation. *Journal of Natural Gas*  
458 *Science and Engineering*, *33*, 1201-1218. <https://doi.org/10.1016/j.jngse.2016.03.042>
- 459 Dayal, P., Savvides, N., & Hoffman, M. (2009). Characterisation of nanolayered aluminium/palladium thin films  
460 using nanoindentation. *Thin Solid Films*, *517*(13), 3698-3703. <https://doi.org/10.1016/j.tsf.2009.01.174>
- 461 Dokukin, M. E., & Sokolov, I. (2012). Quantitative mapping of the elastic modulus of soft materials with HarmoniX  
462 and PeakForce QNM AFM modes. *Langmuir*, *28*(46), 16060-16071. <https://doi.org/10.1021/la302706b>
- 463 Dresselhaus, M. S., Dresselhaus, G., Saito, R., & Jorio, A. (2005). Raman spectroscopy of carbon nanotubes.  
464 *Physics Reports*, *409*(2), 47-99. <https://doi.org/10.1016/j.physrep.2004.10.006>
- 465 Duan, D., Zhang, D., Ma, X., Yang, Y., Ran, Y., & Mao, J. (2018). Chemical and structural characterization of  
466 thermally simulated kerogen and its relationship with microporosity. *Marine and Petroleum Geology*, *89*, 4-13.  
467 <https://doi.org/10.1016/j.marpetgeo.2016.12.016>
- 468 Eliyahu, M., Emmanuel, S., Day-Stirrat, R. J., & Macaulay, C. I. (2015). Mechanical properties of organic matter in  
469 shales mapped at the nanometer scale. *Marine and Petroleum Geology*, *59*, 294-304.

- 470 <https://doi.org/10.1016/j.marpetgeo.2014.09.007>
- 471 Emmanuel, S., Eliyahu, M., Day-Stirrat, R. J., Hofmann, R., & Macaulay, C. I. (2016). Impact of thermal maturation  
472 on nano-scale elastic properties of organic matter in shales. *Marine and Petroleum Geology*, *70*, 175-184.  
473 <https://doi.org/10.1016/j.marpetgeo.2015.12.001>
- 474 Epshtein, S. A., Borodich, F. M., & Bull, S. J. (2015). Evaluation of elastic modulus and hardness of highly  
475 inhomogeneous materials by nanoindentation. *Applied Physics A*, *119*(1), 325-335. [https://doi.org/10.1007/s00339-](https://doi.org/10.1007/s00339-014-8971-5)  
476 [014-8971-5](https://doi.org/10.1007/s00339-014-8971-5)
- 477 Ferrari, A. C., Meyer, J., Scardaci, V., Casiraghi, C., Lazzeri, M., Mauri, F., Piscanec, S., Jiang, D., Novoselov, K., &  
478 Roth, S. (2006). Raman spectrum of graphene and graphene layers. *Physical Review Letters*, *97*(18), 187401.  
479 <https://doi.org/10.1103/PhysRevLett.97.187401>
- 480 Goodarzi, M., Rouainia, M., Aplin, A., Cubillas, P., & de Block, M. (2017). Predicting the elastic response of  
481 organic-rich shale using nanoscale measurements and homogenisation methods. *Geophysical Prospecting*.  
482 <https://doi.org/10.1111/1365-2478.12475>
- 483 Hunt, J. M. (1979). *Petroleum geochemistry and geology*. W H Freemme and Company, San Francisco.
- 484 Hutton, A., Bharati, S., & Robl, T. (1994). Chemical and petrographic classification of kerogen/macerals. *Energy &*  
485 *Fuels*, *8*(6), 1478-1488. <https://doi.org/10.1021/ef00048a038>
- 486 ISO14577-1 (2002). *Metallic materials—instrumented indentation test for hardness and materials parameters*.  
487 International Organization for Standardization, Geneva.
- 488 Jacob, H. (1989). Classification, structure, genesis and practical importance of natural solid oil bitumen  
489 (“migrabitumen”). *International Journal of Coal Geology*, *11*(1), 65-79. [https://doi.org/10.1016/0166-](https://doi.org/10.1016/0166-5162(89)90113-4)  
490 [5162\(89\)90113-4](https://doi.org/10.1016/0166-5162(89)90113-4)
- 491 Jiu, K., Ding, W., Huang, W., You, S., Zhang, Y., & Zeng, W. (2013). Simulation of paleotectonic stress fields within  
492 Paleogene shale reservoirs and prediction of favorable zones for fracture development within the Zhanhua  
493 Depression, Bohai Bay Basin, east China. *Journal of Petroleum Science and Engineering*, *110*, 119-131.  
494 <https://doi.org/10.1016/j.petrol.2013.09.002>
- 495 Johnson, K. L. (1987). *Contact mechanics*. Cambridge University Press.
- 496 Kelemen, S., & Fang, H. (2001). Maturity trends in Raman spectra from kerogen and coal. *Energy & Fuels*, *15*(3),  
497 653-658. <https://doi.org/10.1021/ef0002039>

- 498 Koch, T., Kogler, F. R., Schubert, U., & Seidler, S. (2007). Mechanical properties of organic-inorganic hybrid  
499 materials determined by indentation techniques. *Monatshefte für Chemie-Chemical Monthly*, 138(4), 293-299.  
500 <https://doi.org/10.1007/s00706-007-0612-7>
- 501 Kumar, V., Sondergeld, C. H., & Rai, C. S. (2012). *Nano to macro mechanical characterization of shale*. Paper  
502 presented at SPE Annual Technical Conference and Exhibition, Society of Petroleum Engineers.  
503 <https://doi.org/10.2118/159804-ms>
- 504 Li, C., Ostadhassan, M., Gentzis, T., Kong, L., Carvajal-Ortiz, H., & Bubach, B. (2018). Nanomechanical  
505 characterization of organic matter in the Bakken formation by microscopy-based method. *Marine and Petroleum*  
506 *Geology*, 96, 128-138. <https://doi.org/10.1016/j.marpetgeo.2018.05.019>
- 507 Liu, Y., Xiong, Y., Liu, K., Yang, C., & Peng, P. (2019). Indentation size and loading rate sensitivities on mechanical  
508 properties and creep behavior of solid bitumen. *International Journal of Coal Geology*, 216, 103295.  
509 <https://doi.org/10.1016/j.coal.2019.103295>
- 510 Lünsdorf, N. K. (2016). Raman spectroscopy of dispersed vitrinite—Methodical aspects and correlation with  
511 reflectance. *International Journal of Coal Geology*, 153, 75-86. <https://doi.org/10.1016/j.coal.2015.11.010>
- 512 Naizhen, L., & Guoyong, W. (2016). Shale gas sweet spot identification and precise geo-steering drilling in Weiyuan  
513 Block of Sichuan Basin, SW China. *Petroleum Exploration and Development*, 43(6), 1067-1075.  
514 [https://doi.org/10.1016/S1876-3804\(16\)30124-0](https://doi.org/10.1016/S1876-3804(16)30124-0)
- 515 Oliver, W. C., & Pharr, G. M. (1992). An improved technique for determining hardness and elastic modulus using  
516 load and displacement sensing indentation experiments. *Journal of Materials Research*, 7(06), 1564-1583.  
517 <https://doi.org/10.1557/jmr.1992.1564>
- 518 Oliver, W. C., & Pharr, G. M. (2004). Measurement of hardness and elastic modulus by instrumented indentation:  
519 Advances in understanding and refinements to methodology. *Journal of Materials Research*, 19(1), 3-20.  
520 <https://doi.org/10.1557/jmr.2004.19.1.3>
- 521 Pharr, G., Oliver, W., & Brotzen, F. (1992). On the generality of the relationship among contact stiffness, contact  
522 area, and elastic modulus during indentation. *Journal of Materials Research*, 7(3), 613-617.  
523 <https://doi.org/10.1557/JMR.1992.0613>
- 524 Pimenta, M., Dresselhaus, G., Dresselhaus, M. S., Cancado, L., Jorio, A., & Saito, R. (2007). Studying disorder in  
525 graphite-based systems by Raman spectroscopy. *Physical Chemistry Chemical Physics*, 9(11), 1276-1290.

526 <http://dx.doi.org/10.1039/B613962K>

527 Rybacki, E., Meier, T., & Dresen, G. (2016). What controls the mechanical properties of shale rocks?–Part II:  
528 Brittleness. *Journal of Petroleum Science and Engineering*, *144*, 39-58. <https://doi.org/10.1016/j.petrol.2016.02.022>

529 Stach, E., Murchison, D., Taylor, G. H., & Zierke, F. (1982). *Stach's textbook of coal petrology*. Borntraeger Berlin.

530 Syed Asif, S., Wahl, K., Colton, R., & Warren, O. (2001). Quantitative imaging of nanoscale mechanical properties  
531 using hybrid nanoindentation and force modulation. *Journal of Applied Physics*, *90*(3), 1192-1200.  
532 <https://doi.org/10.1063/1.1380218>

533 Tissot, B. P., & Welte, D. H. (2013). *Petroleum formation and occurrence*. Springer Science & Business Media.

534 Tong, J., Jiang, X., Han, X., & Wang, X. (2016). Evaluation of the macromolecular structure of Huadian oil shale  
535 kerogen using molecular modeling. *Fuel*, *181*, 330-339. <https://doi.org/10.1016/j.fuel.2016.04.139>

536 Tselev, A., Ivanov, I. N., Lavrik, N. V., Belianinov, A., Jesse, S., Mathews, J. P., Mitchell, G. D., & Kalinin, S. V.  
537 (2014). Mapping internal structure of coal by confocal micro-Raman spectroscopy and scanning microwave  
538 microscopy. *Fuel*, *126*, 32-37. <https://doi.org/10.1016/j.fuel.2014.02.029>

539 Ungerer, P., Collell, J., & Yiannourakou, M. (2014). Molecular modeling of the volumetric and thermodynamic  
540 properties of kerogen: Influence of organic type and maturity. *Energy & Fuels*, *29*(1), 91-105.  
541 <https://doi.org/10.1021/ef502154k>

542 Vranjes, S., Misch, D., Schöberl, T., Kiener, D., Gross, D., & Sachsenhofer, R. F. (2018). Nanoindentation study of  
543 macerals in coals from the Ukrainian Donets Basin. *Advances in Geosciences*, *45*. [https://doi.org/10.5194/adgeo-45-](https://doi.org/10.5194/adgeo-45-73-2018)  
544 [73-2018](https://doi.org/10.5194/adgeo-45-73-2018)

545 Wang, G., & Carr, T. R. (2012). Methodology of organic-rich shale lithofacies identification and prediction: A case  
546 study from Marcellus Shale in the Appalachian basin. *Computers & Geosciences*, *49*, 151-163.  
547 <https://doi.org/10.1016/j.cageo.2012.07.011>

548 Wang, M., Sherwood, N., Li, Z., Lu, S., Wang, W., Huang, A., Peng, J., & Lu, K. (2015). Shale oil occurring  
549 between salt intervals in the Dongpu Depression, Bohai Bay Basin, China. *International Journal of Coal Geology*,  
550 *152*, 100-112. <https://doi.org/10.1016/j.coal.2015.07.004>

551 Wilkins, R. W., Boudou, R., Sherwood, N., & Xiao, X. (2014). Thermal maturity evaluation from inertinites by  
552 Raman spectroscopy: the 'RaMM' technique. *International Journal of Coal Geology*, *128*, 143-152.  
553 <https://doi.org/10.1016/j.coal.2014.03.006>

- 554 Wilkinson, T. M., Zargari, S., Prasad, M., & Packard, C. E. (2015). Optimizing nano-dynamic mechanical analysis  
555 for high-resolution, elastic modulus mapping in organic-rich shales. *Journal of Materials Science*, 50(3), 1041-1049.  
556 <https://doi.org/10.1007/s10853-014-8682-5>
- 557 Wu, T., & Firoozabadi, A. (2020). Mechanical properties and failure envelope of kerogen matrix by molecular  
558 dynamics simulations. *The Journal of Physical Chemistry C*. <https://doi.org/10.1021/acs.jpcc.9b09639>
- 559 Yang, J., Hatcherian, J., Hackley, P. C., & Pomerantz, A. E. (2017). Nanoscale geochemical and geomechanical  
560 characterization of organic matter in shale. *Nature Communications*, 8(1), 2179. [https://doi.org/10.1038/s41467-017-](https://doi.org/10.1038/s41467-017-02254-0)  
561 [02254-0](https://doi.org/10.1038/s41467-017-02254-0)
- 562 Zargari, S., Prasad, M., Mba, K. C., & Mattson, E. D. (2013). Organic maturity, elastic properties, and textural  
563 characteristics of self resourcing reservoirs. *Geophysics*, 78(4), D223-D235. <https://doi.org/10.1190/geo2012-0431.1>
- 564 Zargari, S., Wilkinson, T. M., Packard, C. E., & Prasad, M. (2016). Effect of thermal maturity on elastic properties  
565 of kerogen. *Geophysics*, 81(2), M1-M6. <https://doi.org/10.1190/geo2015-0194.1>
- 566 Zeszotarski, J. C., Chromik, R. R., Vinci, R. P., Messmer, M. C., Michels, R., & Larsen, J. W. (2004). Imaging and  
567 mechanical property measurements of kerogen via nanoindentation. *Geochimica et Cosmochimica Acta*, 68(20),  
568 4113-4119. <https://doi.org/10.1016/j.gca.2003.11.031>
- 569 Zhang, Y., Lebedev, M., Smith, G., Jing, Y., Busch, A., & Iglauer, S. (2019). Nano-mechanical properties and pore-  
570 scale characterization of different rank coals. *Natural Resources Research*, 1-14. [https://doi.org/10.1007/s11053-](https://doi.org/10.1007/s11053-019-09572-8)  
571 [019-09572-8](https://doi.org/10.1007/s11053-019-09572-8)
- 572 Zhao, J., Zhang, D., Wu, T., Tang, H., Xuan, Q., Jiang, Z., & Dai, C. (2018). Multiscale approach for mechanical  
573 characterization of organic-rich shale and its application. *International Journal of Geomechanics*, 19(1), 04018180.  
574 [https://doi.org/10.1061/\(asce\)gm.1943-5622.0001281](https://doi.org/10.1061/(asce)gm.1943-5622.0001281)
- 575

Figure 1.

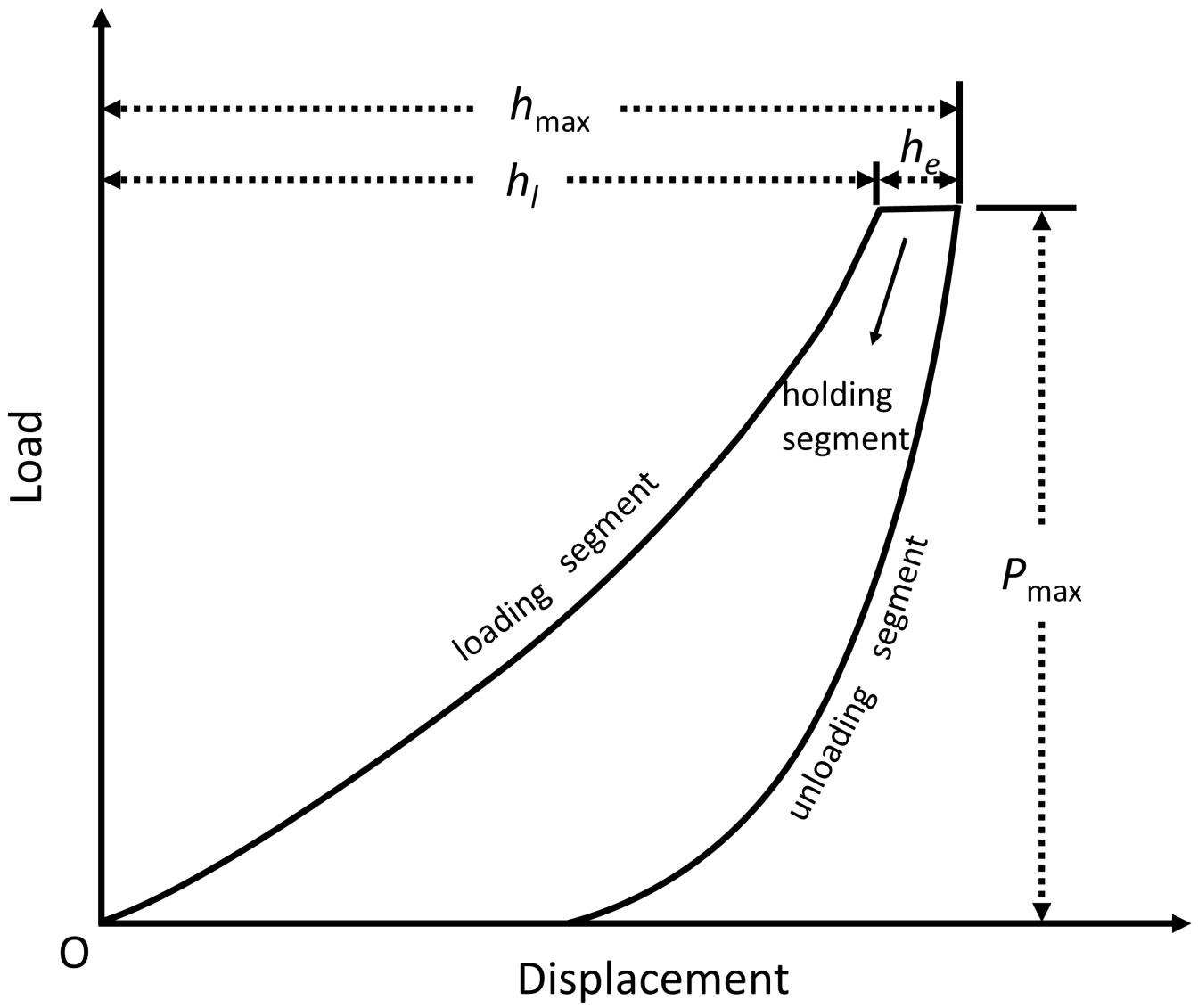


Figure 2.

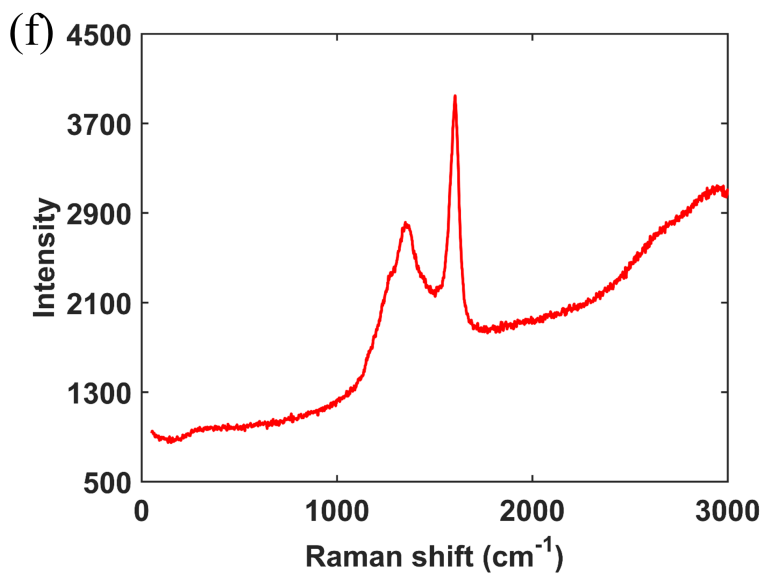
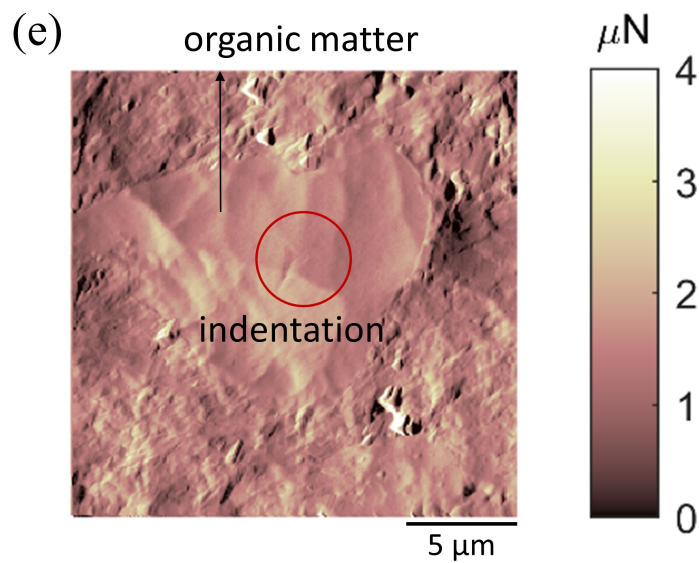
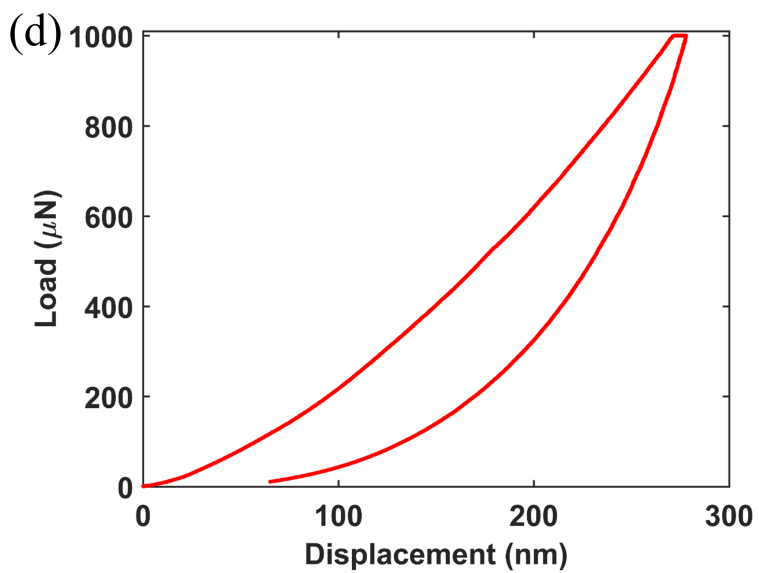
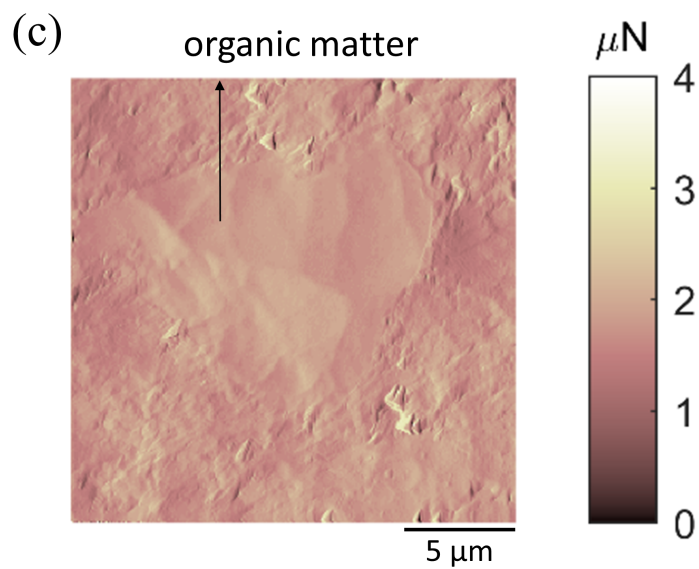
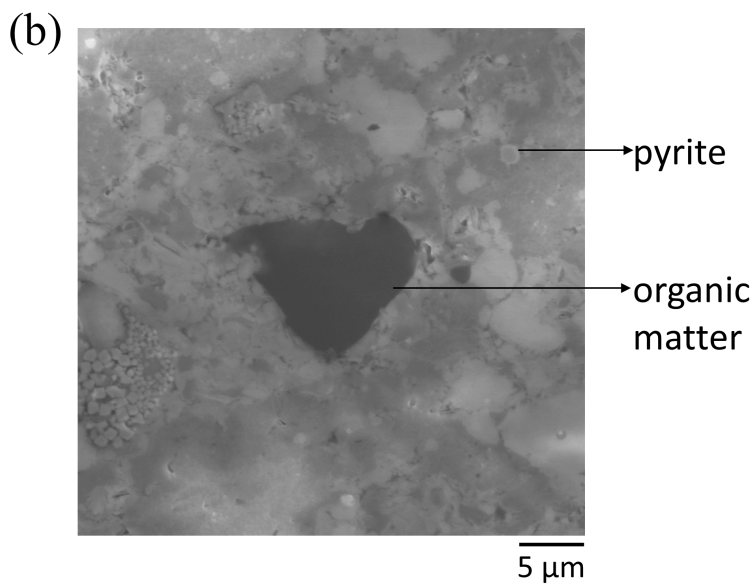
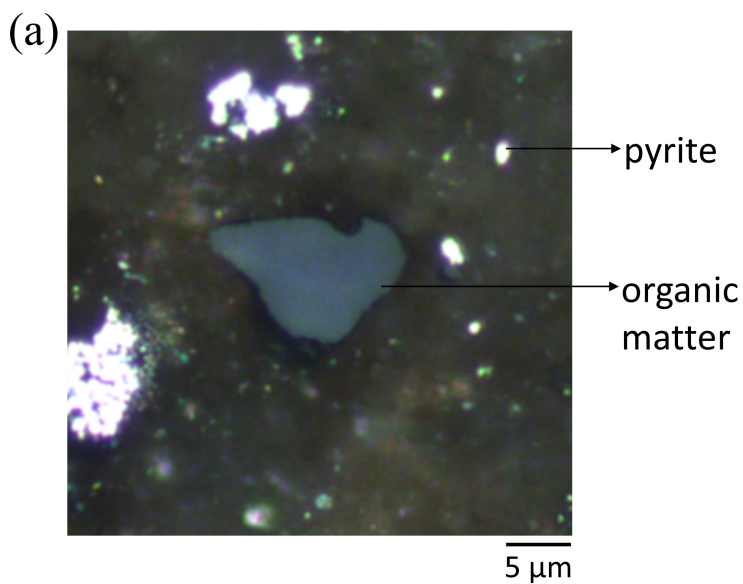
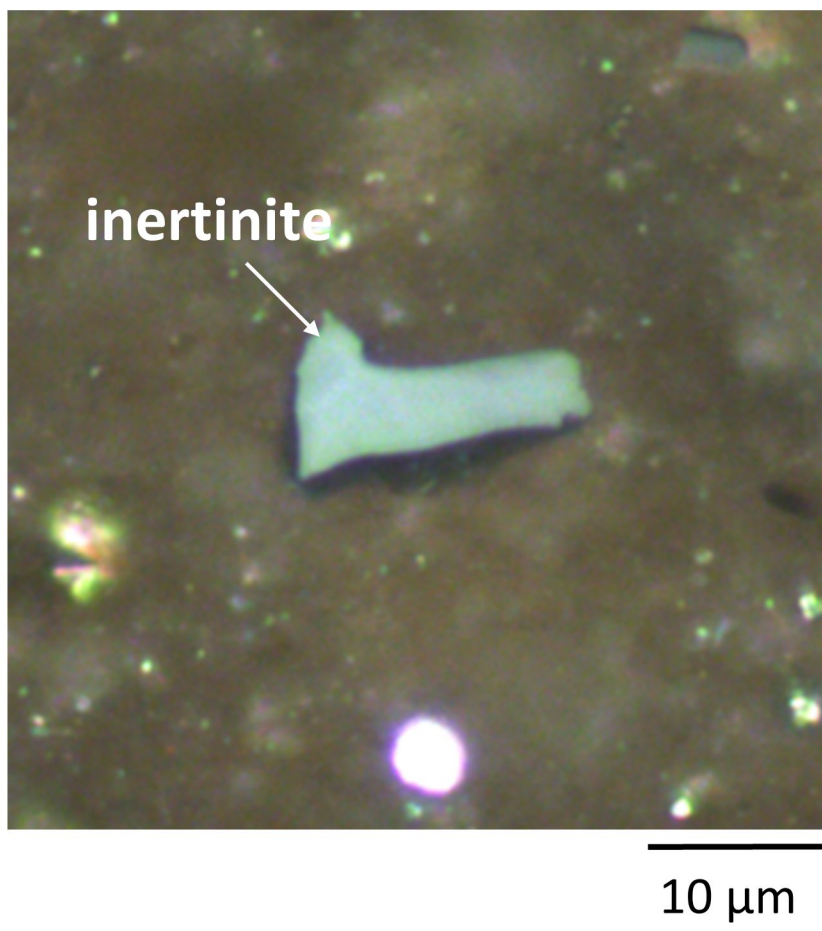
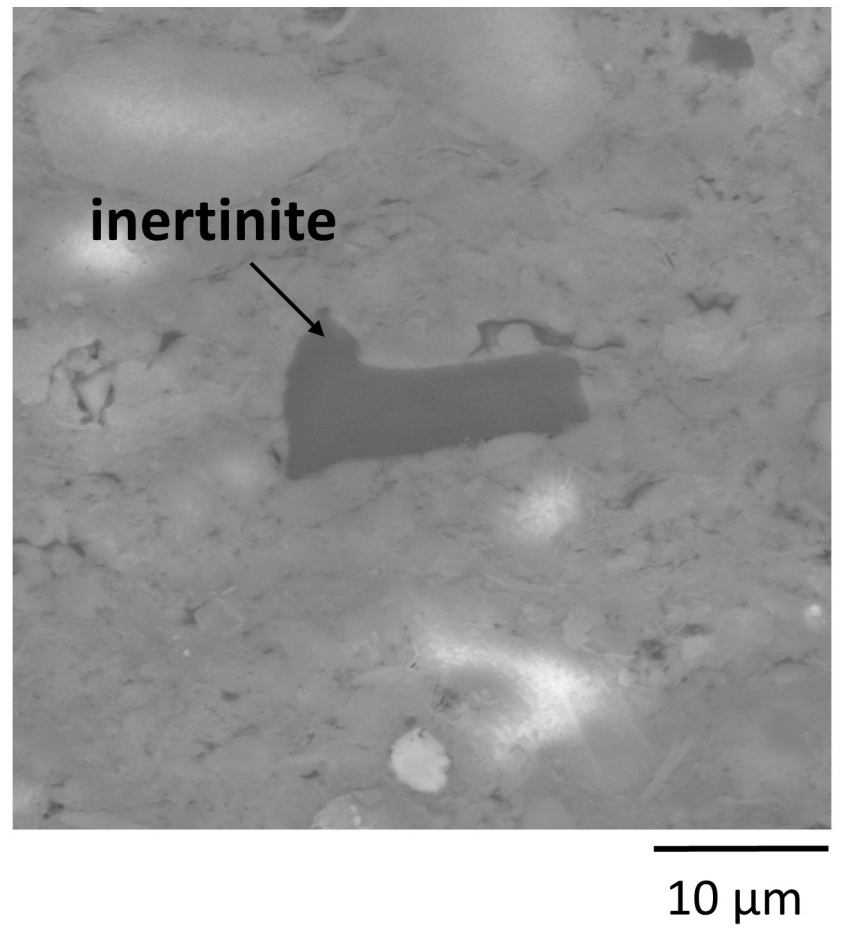


Figure 3.

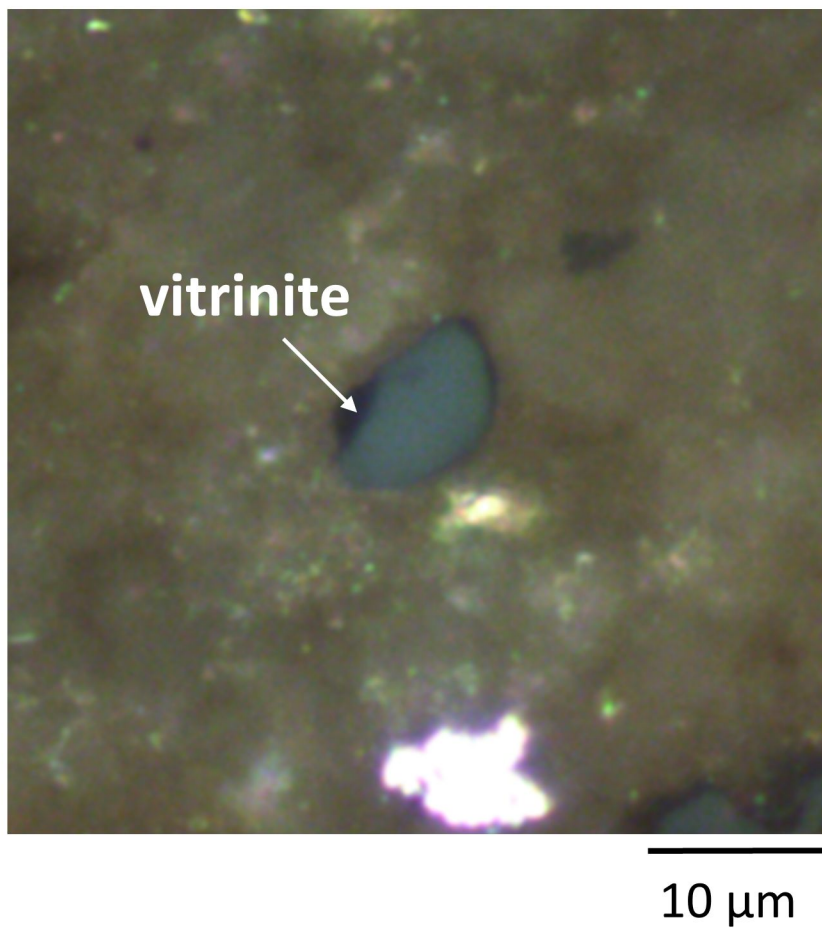
(a)



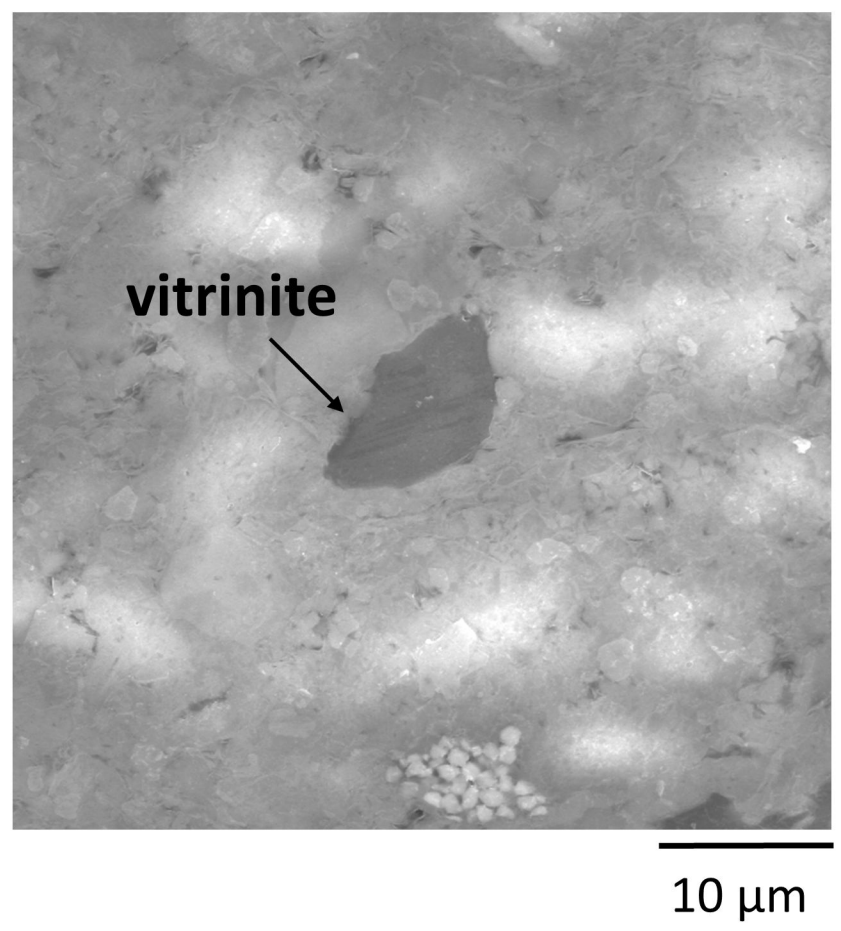
(b)



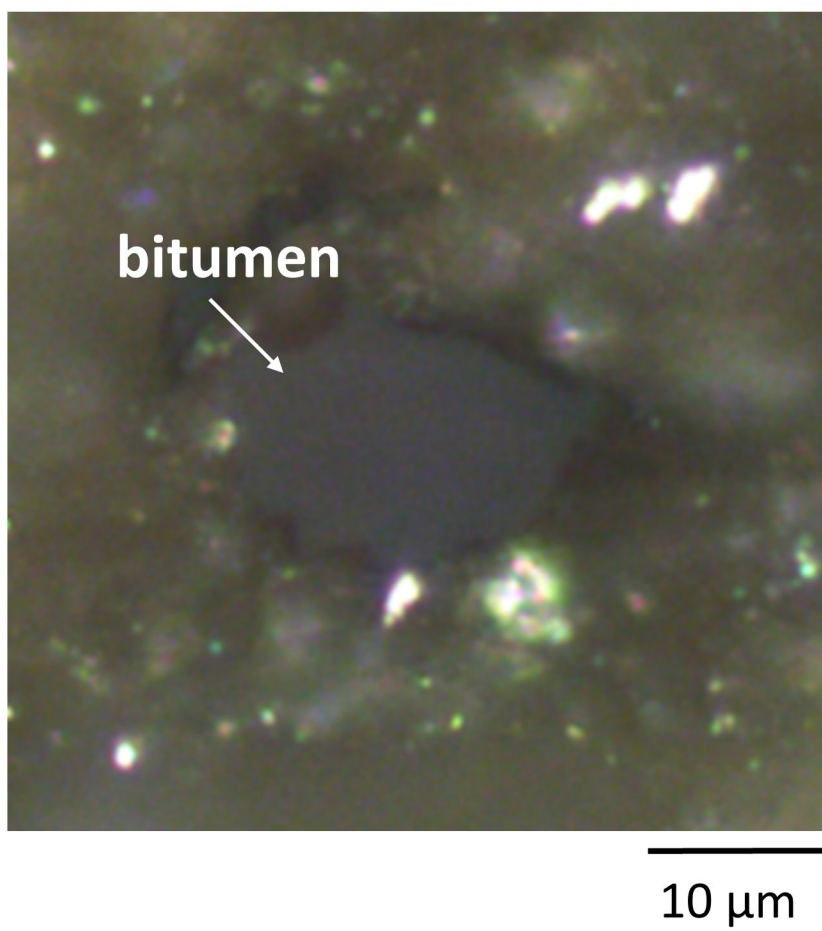
(c)



(d)



(e)



(f)

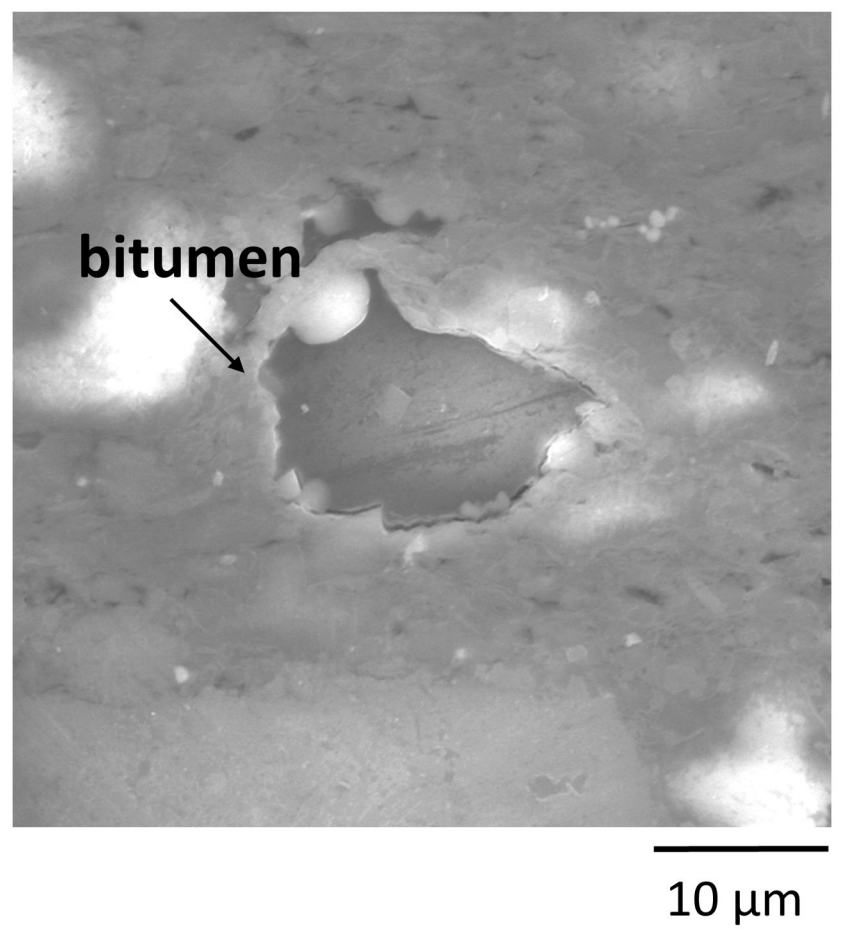


**Figure 4.**

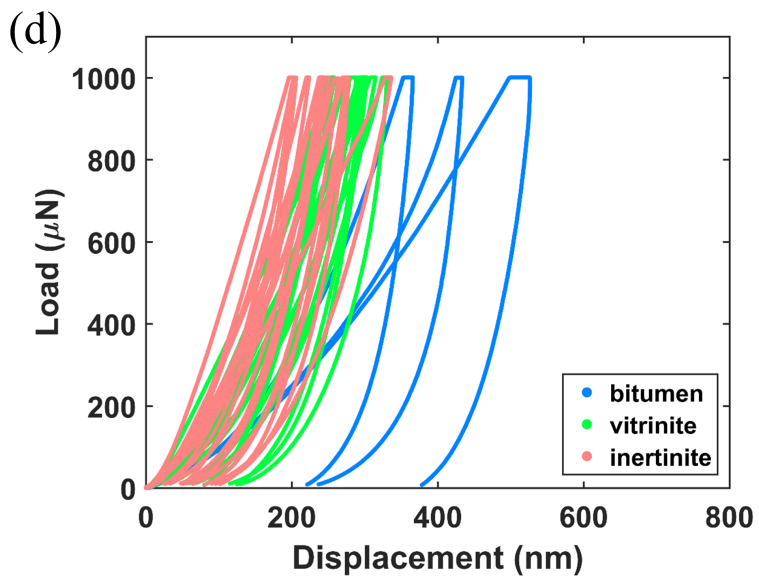
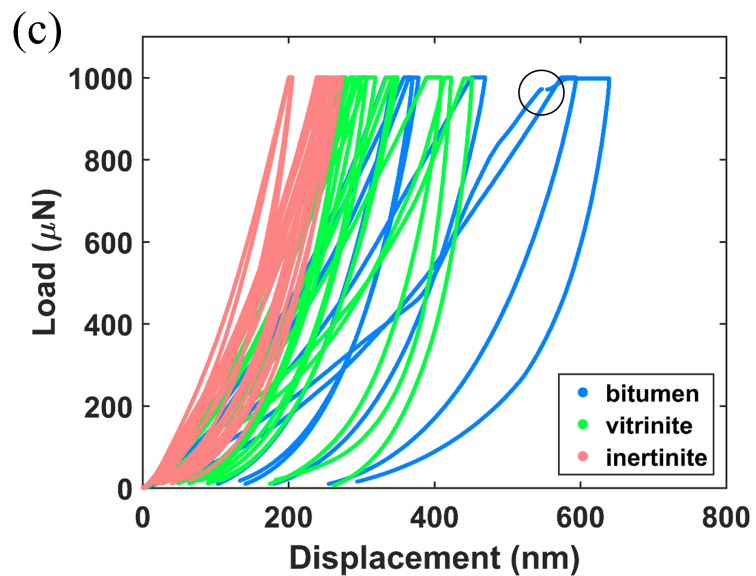
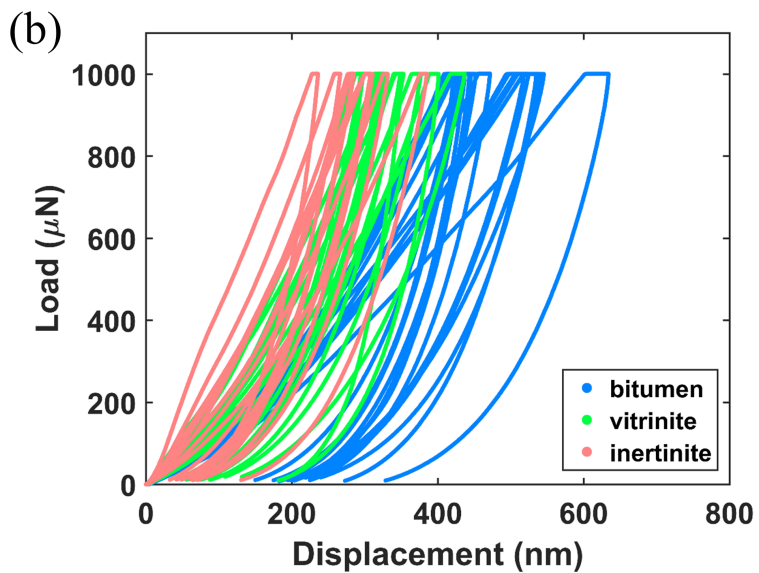
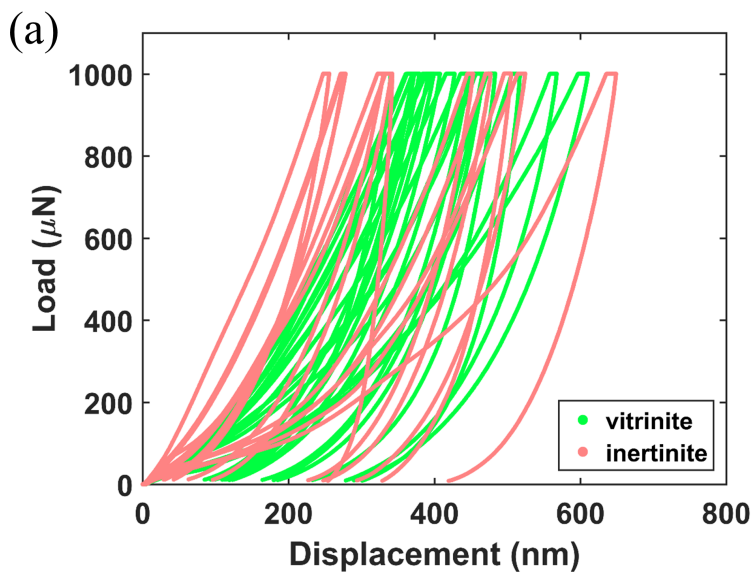


Figure 5.

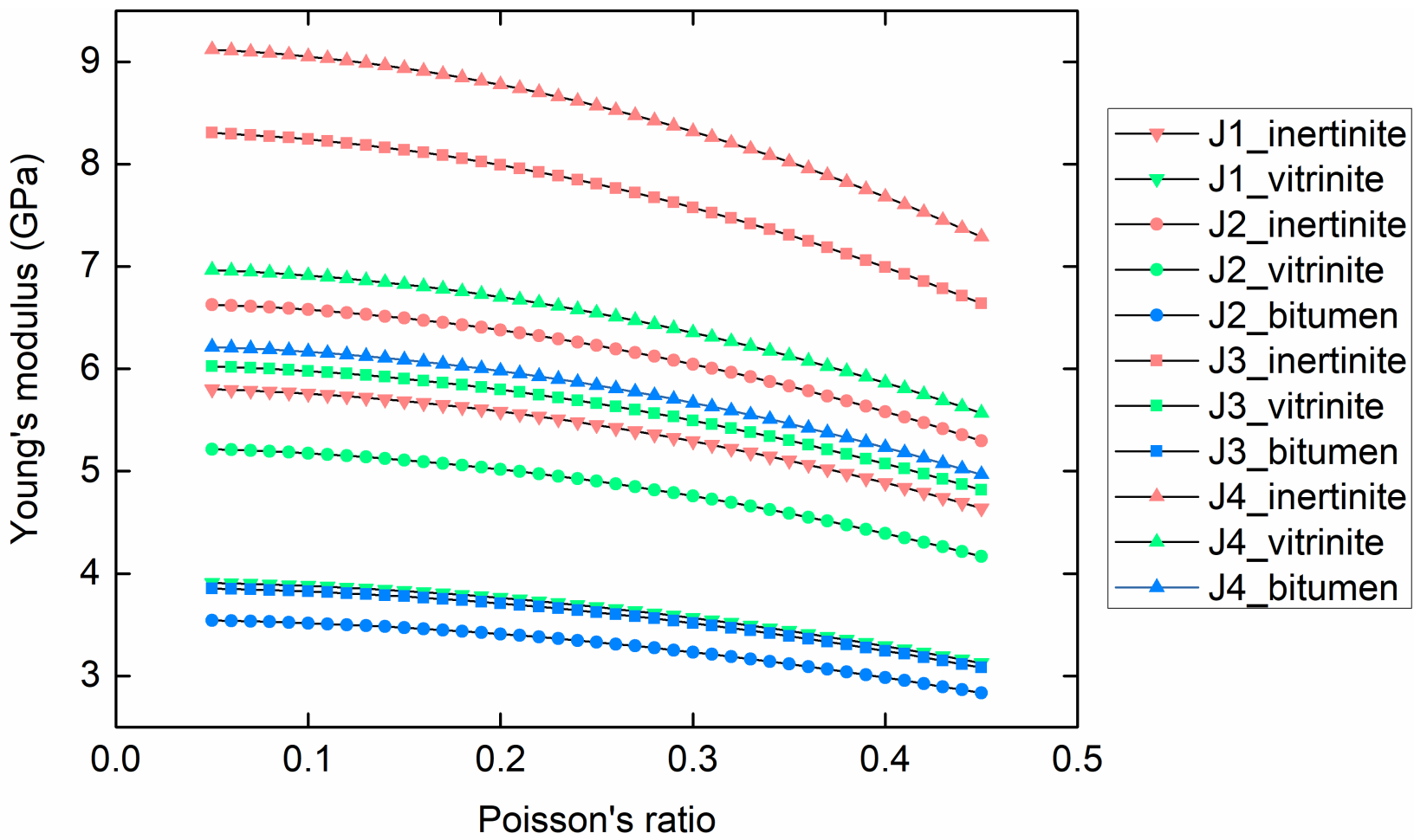


Figure 6.

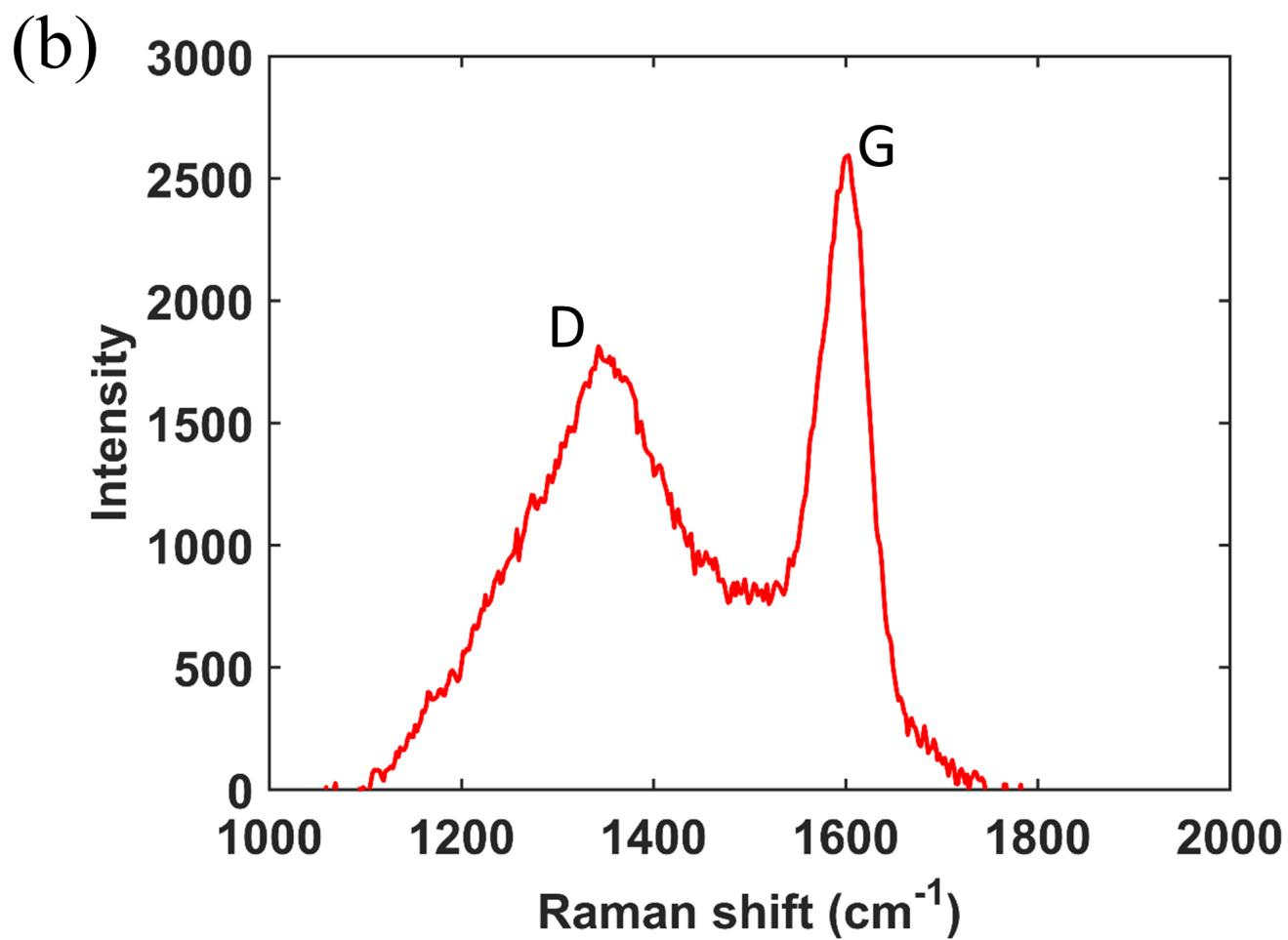
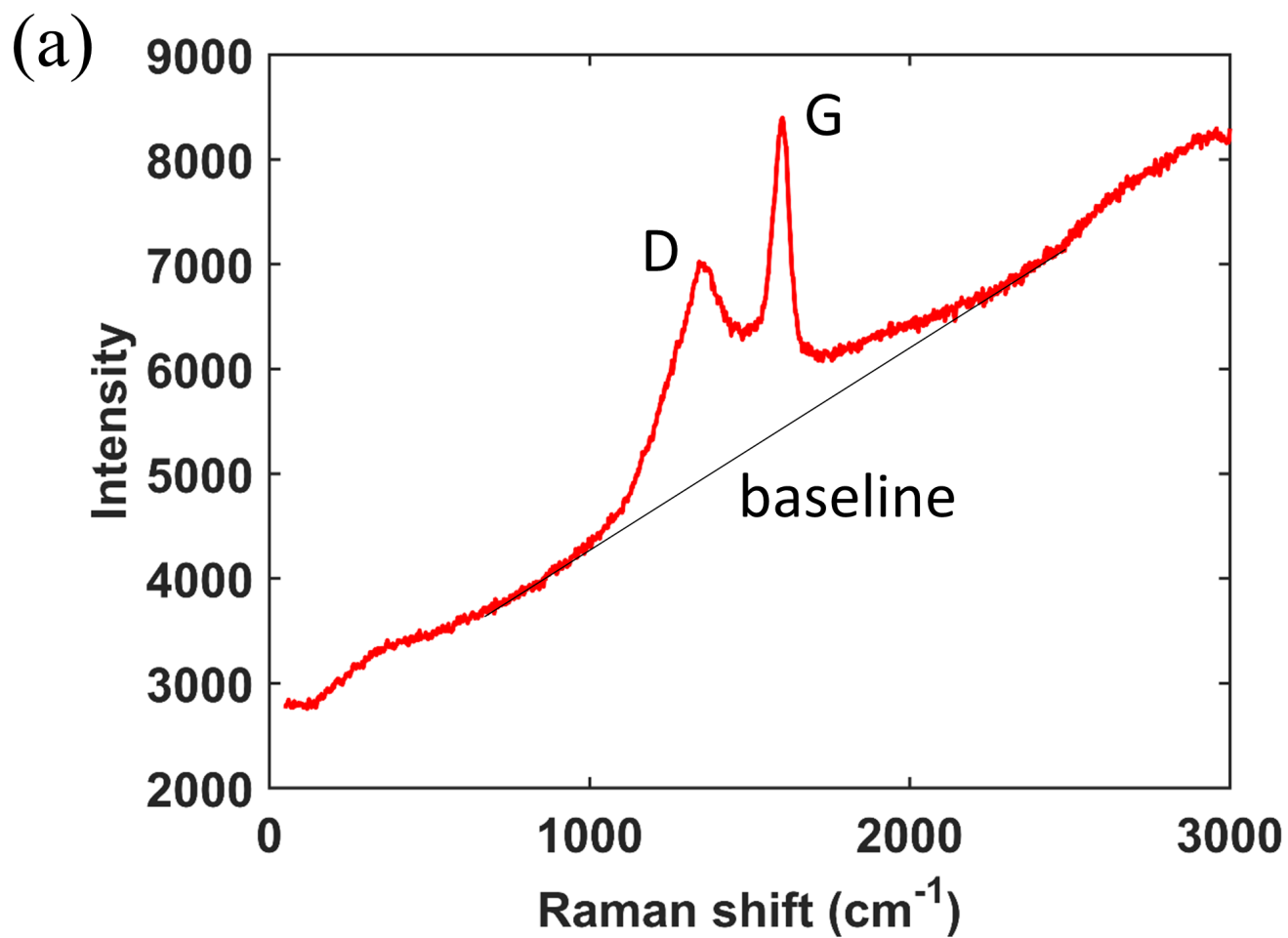
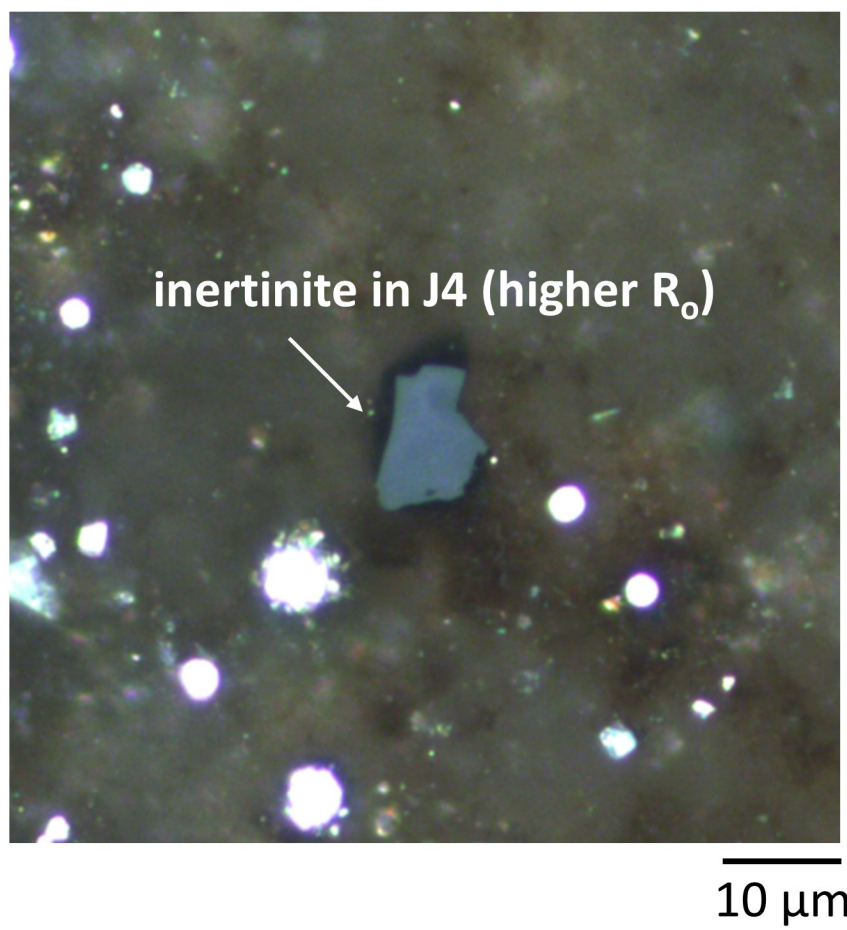
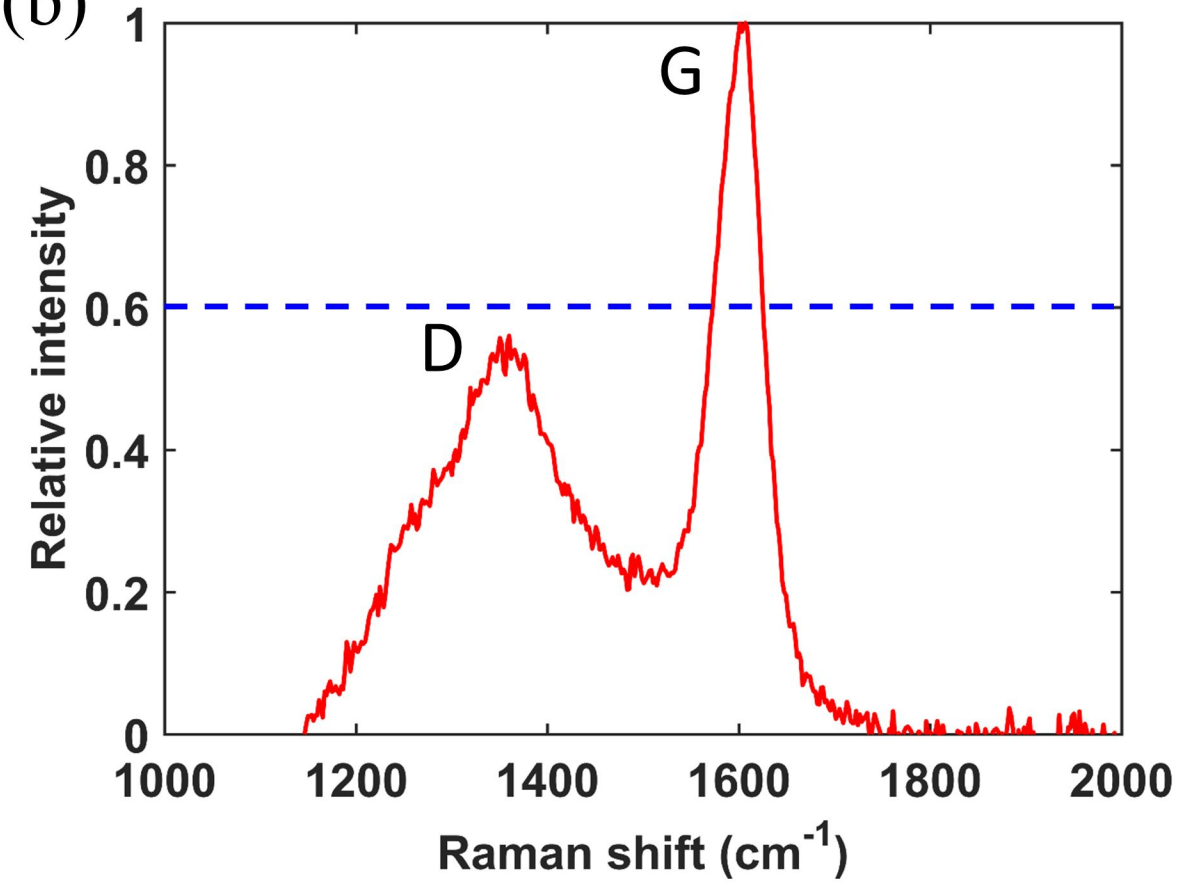


Figure 7.

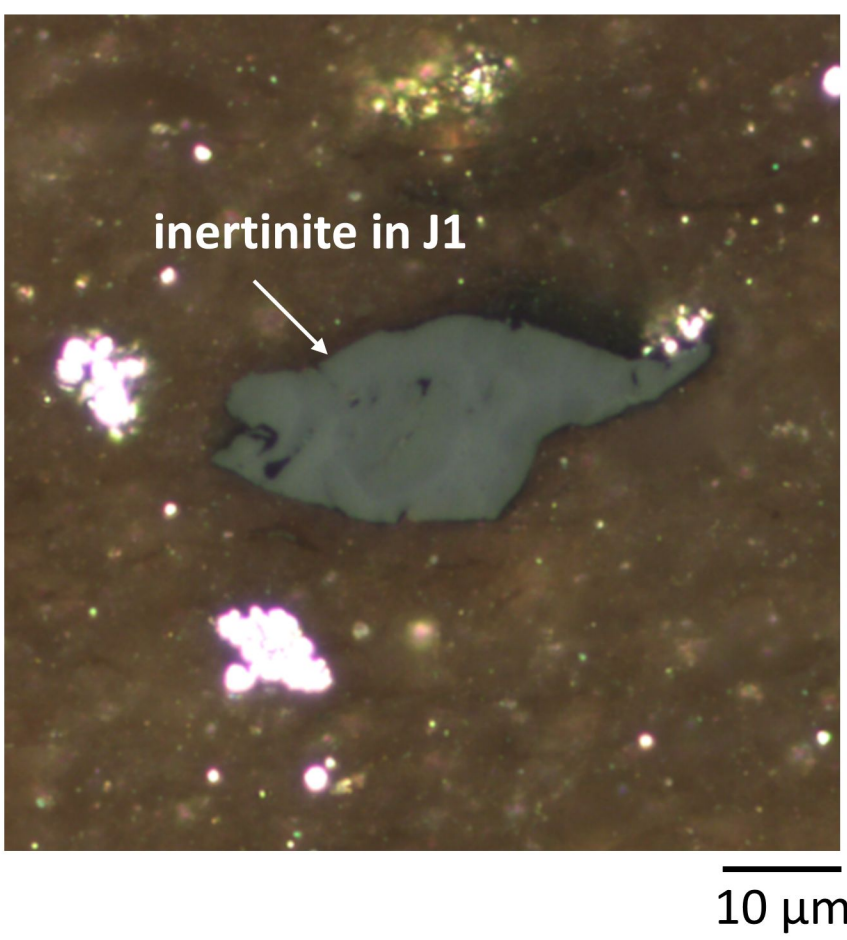
(a)



(b)



(c)



(d)

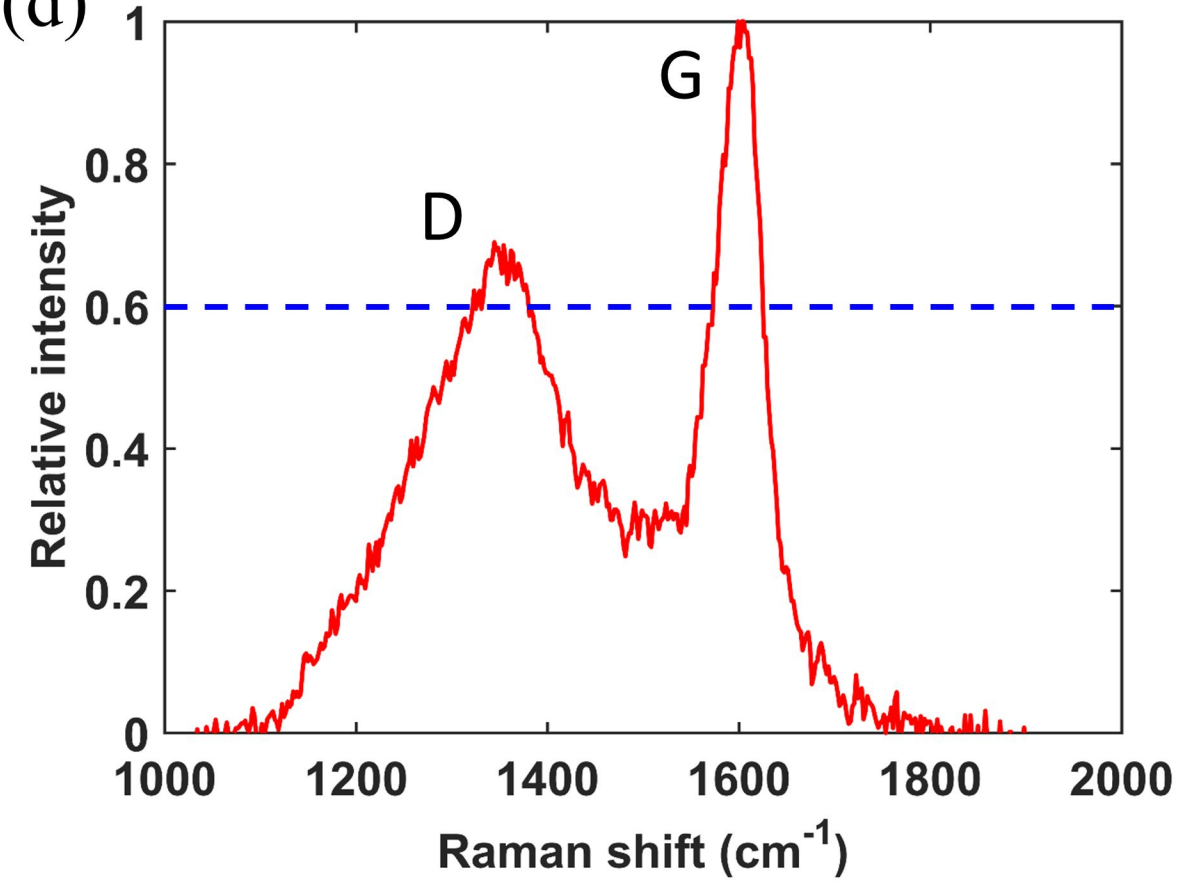


Figure 8.

